Geochemistry, Geophysics, Geosystems®

AGU ADVANCING EARTH AND SPACE SCIENCE

RESEARCH ARTICLE
10.1029/2022GC010830

Key Points:

- Transient weakening of a dry granulite occurred during shearing due to simultaneous inflow of H_2O and diffusional influx of hydrogen
- Spatial phase variations as well as the distribution of water content in a natural sample were used to benchmark a 1D shear zone model
- Model reproduces field-derived shear zone data once the hydrogen influx decreased the wall rock viscosity by around two orders of magnitude

Supporting Information:

Supporting Information may be found in the online version of this article.

Correspondence to:

L. Kaatz and T. John,
lisakaatz@live.de;
timm.john@fu-berlin.de

Citation:

Kaatz, L., Schmalholz, S. M., & John, T. (2023). Numerical simulations reproduce field observations showing transient weakening during shear zone formation by diffusional hydrogen influx and H_2O inflow. *Geochemistry, Geophysics, Geosystems*, *24*, e2022GC010830. https://doi.org/10.1029/2022GC010830

Received 12 DEC 2022
Accepted 25 MAR 2023

Numerical Simulations Reproduce Field Observations Showing Transient Weakening During Shear Zone Formation by Diffusional Hydrogen Influx and H_2O Inflow

L. Kaatz[1], S. M. Schmalholz[2], and T. John[1]

[1]Institute of Geological Sciences, Freie Universität Berlin, Berlin, Germany, [2]Institute of Earth Sciences, University of Lausanne, Lausanne, Switzerland

Abstract Exposures on Holsnøy island (Bergen Arcs, Norway) indicate fluid infiltration through fractures into a dry, metastable granulite, which triggered a kinetically delayed eclogitization, a transient weakening during fluid-rock interaction, and formation of shear zones that widened during shearing. It remains unclear whether the effects of grain boundary-assisted aqueous fluid inflow on the duration of granulite hydration were influenced by a diffusional hydrogen influx accompanying the fluid inflow. To better estimate the fluid infiltration efficiencies and the parameter interdependencies, a 1D numerical model of a viscous shear zone is utilized and validated using measured mineral phase abundance distributions and H_2O-contents in nominally anhydrous minerals of the original granulite assemblage to constrain the hydration by aqueous fluid inflow and diffusional hydrogen influx, respectively. Both hydrations are described with a diffusion equation and affect the effective viscosity. Shear zone kinematics are constrained by the observed shear strain and thickness. The model fits the phase abundance and H_2O-content profiles if the effective hydrogen diffusivity is approximately one order of magnitude higher than the diffusivity for aqueous fluid inflow. The observed shear zone thickness is reproduced if the viscosity ratio between dry granulite and deforming, reequilibrating eclogite is $\sim 10^4$ and that between dry granulite and hydrated granulite is $\sim 10^2$. The results suggest shear velocities $<10^{-2}$ cm/a, hydrogen diffusivities of $\sim 10^{-13\pm1}$ m^2/s, and a shearing duration of <10 years. This study successfully links and validates field data to a shear zone model and highlights the importance of hydrogen diffusion for shear zone widening and eclogitization.

Plain Language Summary At zones of colliding tectonic plates, rocks of the lower continental crust are sometimes buried down into the Earth's mantle. Due to increasing pressures and temperatures during deep burial, the rock's minerals transform. Hence, to maintain a more stable assemblage, the system continuously reequilibrates via metamorphic mineral reactions and the rock properties, such as strength and density, change. Occasionally, dry crustal rocks can resist such processes and are transported to great depths without any transformation and reequilibration. If fluid enters such a metastable system, the rock properties can change, transforming transiently from rigid to weak and enabling ductile deformation. Based on one such example from Western Norway, this work studies the effects of H_2O inflow and hydrogen influx on the rock viscosity with the help of a 1D mathematical model, where measurements from the rock were used to constrain and validate the model. The results show the most likely conditions that the rock faced in terms of shear velocity, fluid diffusivity, and the duration of deformation.

1. Introduction

During the collision of tectonic plates, descending crustal rocks are exposed to increasing pressures (P) and temperatures (T), which initiate metamorphism facilitating viscous deformation or vice versa (e.g., Klemd et al., 2011; Schneider et al., 2013; Yuan et al., 2000). However, in the case of dry and therefore rigid protoliths, as they are common in the lower crust, some parts undergo neither ductile deformation nor metamorphism during burial, as long they are not affected by the influx of an externally derived fluid (e.g., Austrheim, 1987; Jackson et al., 2004; Jamtveit, Moulas, et al., 2018; Jamtveit et al., 2019; John & Schenk, 2003; Mancktelow & Pennacchioni, 2005; Menegon et al., 2017; Putnis & Austrheim, 2010; Putnis & John, 2010). Hence, these rocks maintain metastable during burial until fluid triggers mineral reactions, as fluids are known to promote equilibration and deformation (e.g., Austrheim, 1987; Hobbs et al., 2008; John & Schenk, 2003; Katayama & Karato, 2008; Pennacchioni & Mancktelow, 2007; Putnis, 2021; Stünitz et al., 2020).

Beside others, for example, Bucher and Grapes (2009), Menegon et al. (2008), and Wayte et al. (1989), Holsnøy island (Bergen Arcs, Norway) is a key locality for such a situation, whereby a metastable dry granulite was infiltrated by an aqueous fluid, triggering eclogite-facies equilibration of the rock (e.g., Austrheim, 1987; Jolivet et al., 2005; Kaatz et al., 2022; Zertani et al., 2019). Here, mineral reactions initiated by fluid infiltration (e.g., Austrheim, 1987; Zertani et al., 2022) enable a concise transient weakening of the granulite only during reequilibration reactions and facilitate to its viscous deformability (e.g., Austrheim, 1987; Bras et al., 2021; Kaatz et al., 2021; Moulas et al., 2022; Raimbourg et al., 2005). The result is a network of eclogite-facies shear zones of various scales.

For the rocks exposed on Holsnøy, fluid became available for the buried granulite unit presumably by the inflow through fractures (e.g., Austrheim, 1987; Jamtveit, Ben-Zion, et al., 2018). Recently, Kaatz et al. (2022) demonstrated that the fluid infiltration into the granulite occurred via two different types of contemporaneous hydration processes: (a) A porous inflow of aqueous fluid, which enabled mineral reactions and, thus, reequilibration to eclogite-facies conditions. (b) This porous inflow was accompanied by a faster, pervasive diffusional hydrogen influx, which hydrated the granulite mineral assemblage. Several authors have shown that any aqueous fluid, including subduction zone fluids, are dissociated, which means they predominantly consist of H_2O and trace amounts of OH^-, H^+, and H_2 (e.g., Manning, 2004; Manning & Frezzotti, 2020; Piccoli et al., 2019; Zheng & Hermann, 2014). Here, the influx of hydrogen was probably much faster and likely more pervasive compared to the H_2O inflow (e.g., Dohmen & Milke, 2010; P. Tollan & Hermann, 2019). The diffusional hydrogen influx is mainly controlled by grain-boundary diffusion but especially occurs via volume diffusion through the grain interiors, as described in, for example, Dohmen and Milke (2010). The inflow of H_2O was certainly grain-boundary assisted and possibly driven by the high chemical potential of the reactive metastable granulite and/or by fluid pressure gradients (e.g., Llana-Fúnez et al., 2012; Malvoisin et al., 2015; Plümper et al., 2017; Zertani et al., 2022).

The aim of this study is to understand how and if the hydrogen influx affected the equilibration and deformation process on Holsnøy island. Therefore, the rock-forming minerals and how they could be affected by hydrogen diffusion are considered first. The minerals constituting the granulite mineral assemblage are mainly nominally anhydrous minerals (NAMs), where plagioclase (plg) constitutes large volumes of approximately 60 vol.% (e.g., Austrheim, 1987; Kaatz et al., 2022; Zertani et al., 2019). Importantly, Kaatz et al. (2022) showed that plg breaks down after limited hydrogen incorporation, causing a matrix grain-size minimization along with the formation of hydrated plg and clinozoisite (czs). Furthermore, studies have shown that hydrogen in the crystal lattice reduces the activation energy of creep mechanisms, especially climb, for example, in olivine (e.g., De Ronde et al., 2005; Mackwell & Kohlstedt, 1990; Mackwell et al., 1990). At the Holsnøy site, these effects may have contributed to the transient weakening and shear zone formation (e.g., Herwegh et al., 2008; Kaatz et al., 2022). In general, plg is the most abundant phase in crustal rocks and, hence, determines their mechanical strength and deformability (e.g., Behrens, 2021; Mosenfelder et al., 2015; Rybacki & Dresen, 2000, 2004). Consequently, it is feasible that a fast, pervasive hydrogen influx accompanying an aqueous fluid inflow influenced the hydration, eclogitization, strength, and deformation on Holsnøy. However, only limited data are available to indicate that a hydrogen influx boosts these processes due to the uptake of hydrogen in plg as well as in other NAMs constituting crustal rocks.

Recently, it has been suggested that the fluid infiltration on Holsnøy can be sufficiently approximated via bulk diffusion of aqueous fluid, mainly H_2O, with bulk diffusivities of $D_b = 10^{-14\pm2}$ m^2/s (e.g., Bras et al., 2021; Kaatz et al., 2021). Assuming such diffusivities, Bras et al. (2021) provided viscosity, η, ratios during progressive shearing, eclogitization, and hydration of $\eta_{transient}/\eta_{granulite} < 1$ and $\eta_{transient}/\eta_{eclogite} < 1$. However, an additional hydrogen influx accompanying the H_2O inflow (e.g., Kaatz et al., 2022) might influence how hydration propagates into the wall rock and how it impacts the rheological behavior of the affected rocks. It is necessary to understand how and to what extent the diffusional hydrogen influx changes the petrological rock properties, for example, the effective viscosities of the system.

Therefore, the first aim of this study is to quantify how the hydrogen influx affects the effective viscosities during reequilibration to eclogite-facies mineral assemblage and contemporaneous deformation. Furthermore, the target is to decipher how fast both influxes are and to evaluate previously published diffusivities. Another aim is to quantify the duration of the hydration and deformation process that led to the formation of a cm-scale shear zone. To accomplish this, a comprehensive data set including mineral phase abundances, H_2O-content distribution and geometrical data is used as a reference to be replicated by a simple 1D numerical shear zone model. Overall, determining the extent of potential hydrogen-induced temporary weakening is crucial for understanding the fluid-induced weakening of subducting continental crust.

2. Case Study: Holsnøy

Holsnøy is located in western Norway and is part of the Bergen Arc System, which was formed during the Caledonian orogeny due to the collision of Baltica and Laurentia (e.g., Andersen et al., 1991; Corfu et al., 2014; Fossen & Dunlap, 1998; Hacker et al., 2010; Roberts, 2003). As a result, a complex structure of subsequently southeastward-thrusted tectonic nappes was built mainly composed of middle Proterozoic anorthositic granulite, mangarites, jotunites, and metagabbros (e.g., Austrheim & Griffin, 1985; Jakob et al., 2017). These lithologies partially experienced Caledonian eclogite-to-amphibolite-facies metamorphism at ∼430 ± 3.5 Ma (Glodny et al., 2008) and at conditions of approximately 2 GPa and ∼700°C (e.g., Bhowany et al., 2018; Jamtveit et al., 1990).

At the elevated P-T conditions, the dry granulite-facies wall rocks of Holsnøy were fractured, which enabled very localized fluid flow (e.g., Austrheim, 1987; Jamtveit, Ben-Zion, et al., 2018; Jamtveit et al., 1990; Petley-Ragan et al., 2018). It has been suggested that the fluid was derived either from sedimentary rocks undergoing devolatilization during the Caledonian orogeny (Andersen et al., 2012; Jakob et al., 2017; Mattey et al., 1994) or by partial melting of schists and anorthositic granulites at the base of the nappe pile (e.g., Austrheim & Boundy, 1994; Jamtveit et al., 2021). Subsequently, fluid-rock interaction and fluid infiltration into the granulites triggered eclogitization, which mechanically weakened the metastable granulite within discrete zones, whereby the fluid availability was a limiting factor for the extent of eclogitization and the eclogite distribution (e.g., Austrheim, 1987; Labrousse et al., 2010; Raimbourg et al., 2007; Zertani et al., 2019).

As soon as the granulite was sufficiently weakened and metamorphic reactions were initiated, the hydrated zones were susceptible to ductile deformation and eclogite-facies shear zones could form (e.g., Boundy et al., 1992; Kaatz et al., 2021; Putnis & Austrheim, 2010; Raimbourg et al., 2005). During progressive deformation, shear zones evolve, widen due to a sufficient fluid supply and infiltration, and form an interconnected network of cm- to km-scale eclogite-facies shear zones (e.g., Austrheim, 1987; Fountain et al., 1994; Kaatz et al., 2021). However, a heterogeneous hydration caused an extremely heterogeneous distribution of eclogite abundances (Figure 1b; e.g., Austrheim & Griffin, 1985; Boundy et al., 1992; Jolivet et al., 2005; Zertani et al., 2019).

2.1. Incipient Eclogitization of the Granulite Wall Rock

By examining the cross-sectional sample of Kaatz et al. (2022) with a cm-scale eclogite-facies shear zone and its granulitic wall rock (Figures 2a–2c), it became evident that the hydration progressively transposed the granulitic wall rock, as different microstructures and grain sizes are observed depending on the distance from the shear zone (Figure 3). The following descriptions and interpretations are mainly based on the analysis of Kaatz et al. (2022) but are similar to those described by various studies on Holsnøy (e.g., Austrheim, 1987; Boundy et al., 1992; Jamtveit et al., 1990; Putnis, 2021; Zertani et al., 2019).

The granulite has grain sizes of approximately 1 mm for grt and plg and >2 mm for the cpx (Figures 3a, 3e, and 3i). The grt grains are isometric, have a homogenous pyrope-rich composition (∼$Alm_{29}Pyr_{52}Grs_{19}$), and are often fractured. Cpx (diopsidic to augitic) occurs within coronas often associated with grt and built a pronounced foliation. Plg of labradoritic to andesitic composition ($An_{45}Ab_{54}Or_1$) constitutes ∼60% of the granulite matrix with distinct grain boundaries (Figure 3i).

The transition zone, from eclogite-facies shear zone to dry granulite wall rock, shows czs needles (10–80 μm, Figure 3j), which form along the plg grain boundaries. Czs needles are the first result of incipient eclogitization and increase their abundance toward the eclogite-facies shear zone (Figure 3k) often intergrown with an albite-rich (∼$An_{28}Ab_{71}$) plg (e.g., Incel et al., 2019; Petley-Ragan et al., 2018; Zertani et al., 2022). Czs formation is not limited to the former plg phase boundaries but also occurs within the plg grain interior (Figures 3k and 3l). The grt grains develop an eclogite-facies Fe-rich rim (∼$Alm_{45}Pyr_{36}Grs_{19}$), and lose their isometric shape (Figures 3b and 3c), indicating dissolution and volume loss by element transfer. Especially within the coronas, when the grt is in contact with plg, a reaction rim is formed mainly composed of omph and czs producing an irregular grt rim with angular grain boundaries of ∼120°. This indicates an established equilibrium among the newly formed and recrystallized minerals. The chemical composition of the granulite-facies cpx remains unaltered throughout the entire transition zone. Closer to the shear zone, a reaction rim is formed when the cpx is in contact with plg (Figure 3g); this rim comprises amph, czs, and omph.

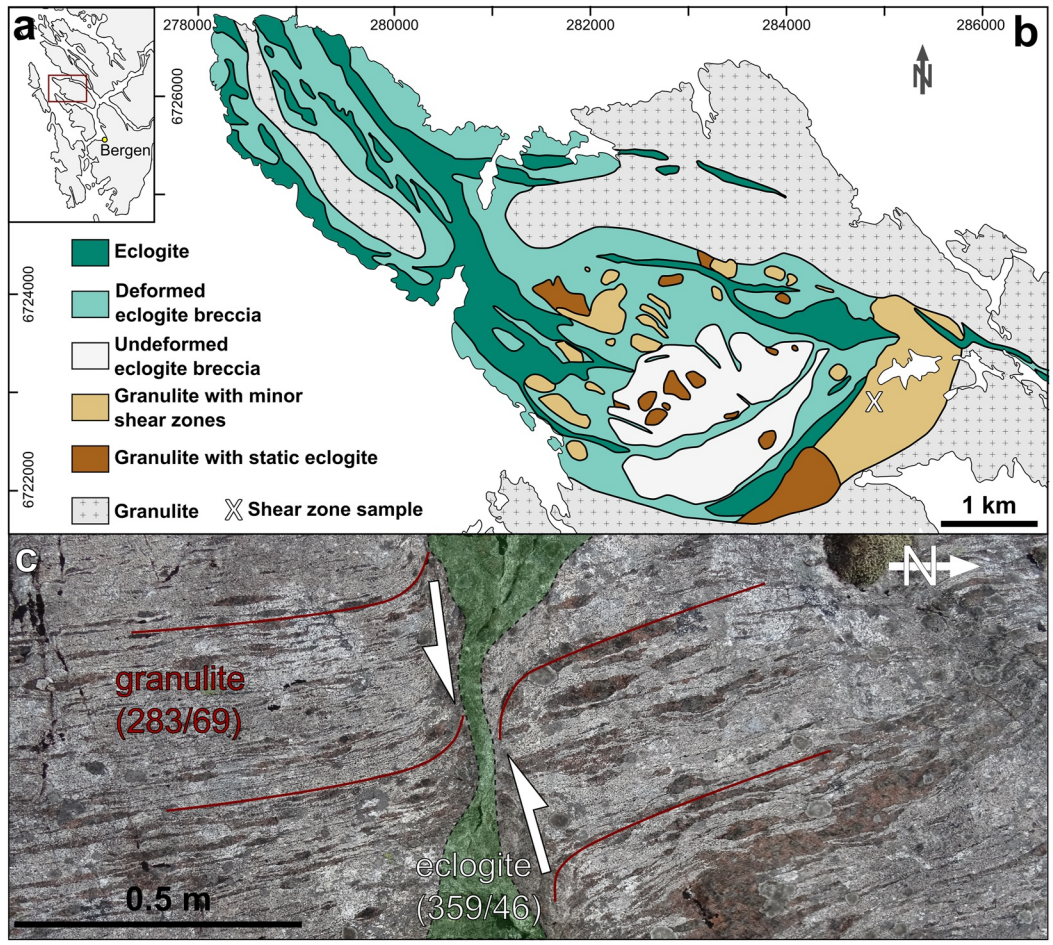

Figure 1. (a) Location of northwest Holsnøy, northwest of Bergen, Norway (red box). (b) Geological map showing the northwestern part of Holsnøy (modified from Zertani et al. (2022)) and its lithological structure with spatially varying eclogitization abundances. (c) Photograph of one representative cm-scale eclogite-facies shear zone (highlighted in green, foliation 359/46). Granulite foliation (red lines, foliation 283/69, lineation shallowly dips to the west) is dragged into the shear zone, indicating sinistral sense of shear. Eclogitization is macroscopically limited to the location of the shear zone.

Only a small fraction of the relict pristine cpx composition is found at the outer part of the eclogite-facies shear zone. The cpx grain size is reduced to approximately 0.5 mm (Figure 3h). The eclogite grt is characterized by irregular rims having a pronounced zonation with a granulite-facies pyrope-rich core (~$Alm_{29}Pyr_{52}Grs_{19}$) and an eclogite-facies almandine-rich rim (~$Alm_{45}Pyr_{36}Grs_{19}$). No plg of granulite-facies composition is left within the eclogite shear zone and hence the matrix is composed of breakdown products, for example, czs, ky, qtz, and amph. These phases have grain sizes of ~10–80 μm (Figure 3l) in the shear zone, which is an immense contrast to the large grain size of the wall rock. From the wall rock to the shear zone, the mineral assemblage changes from granulite to eclogite from anhydrous dominated phases (<500 μg/g bulk H_2O) to hydrous dominated phases (>2,500 μg/g bulk H_2O, Figure 2d).

2.2. Hydration Along the Cross-Section of the Sampled Shear Zone

The H_2O content within the constituting minerals increases toward the shear zone within areas of preserved granulite-facies composition from 10 to 50 μg/g for grt, 100–310 μg/g for cpx, and 10–144 μg/g for plg (e.g., Kaatz et al., 2022; Malvoisin et al., 2020). This H_2O increase is primarily characterized by uptake of hydrogen bound to the oxygen inside the crystal lattice, whereby OH-groups are incorporated by decorating preexisting defects (e.g., Padrón-Navarta et al., 2014; Stalder et al., 2007; P. M. Tollan et al., 2018). The fast transport of hydrogen by grain-boundary and volume diffusion does not necessarily require mineral reactions but

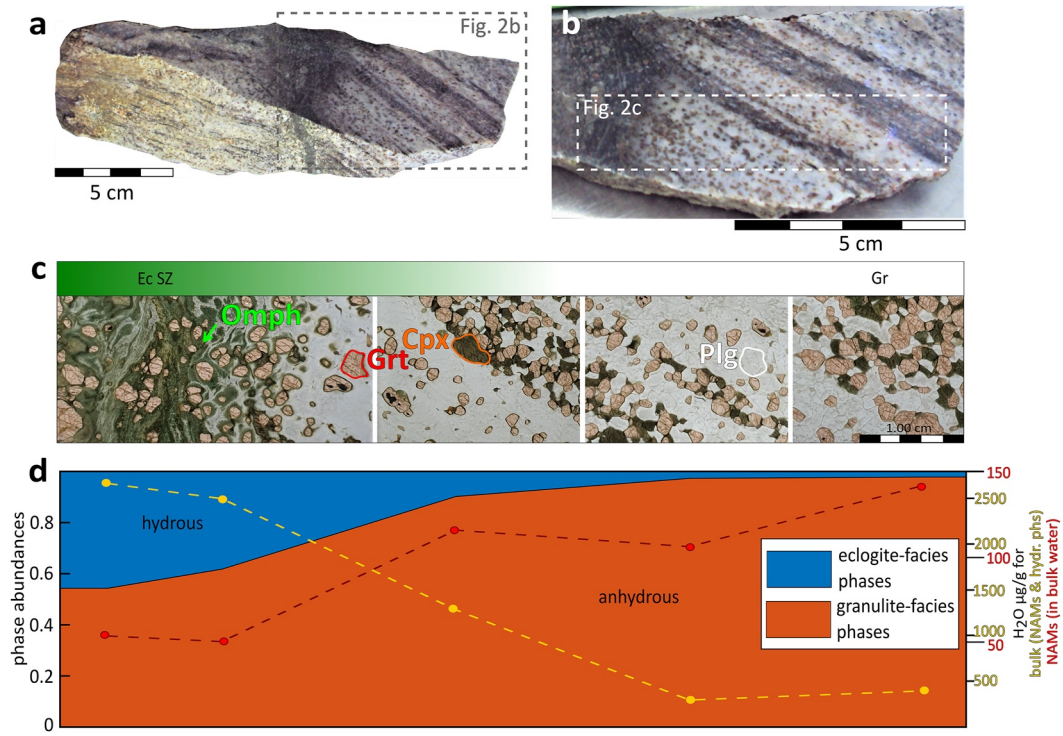

Figure 2. (a) Photograph of the sample analyzed in Kaatz et al. (2022) with a cm-scale localized eclogite-facies shear zone in the center surrounded by almost pristine granulite. (b) Rock slice showing the right part of the sample used for detailed measurements. (c) Continuous thick-section profile showing the transition from granulite to eclogite, which is characterized by different microstructures and abundance of eclogite-facies phases increasing from granulite to the shear zone. Most abundant phases are grt, granulitic plg, cpx, and omph. (d) Plot representing the modal abundance of anhydrous, granulite-facies phases (orange) and hydrous phases (blue). The yellow dashed line gives the bulk H_2O content for the NAMs (grt, cpx, plg), czs, and amph based on their modal abundance. The red dashed curve represents the H_2O content of the NAMs as a portion of the bulk H_2O. This simplified profile shows the progressive eclogitization as a result of successive hydration of the granulitic wall rock.

probably leads to a preweakening of the granulite. Contemporaneously, the slower grain boundary-assisted inflow of aqueous fluid enables element transfer and exchange by dissolution-precipitation mechanisms (e.g., Putnis & John, 2010; Zertani et al., 2022). Hence, the addressed microstructural transformations occur while new eclogite-facies and hydrous minerals form and incorporate OH-groups (e.g., Kaatz et al., 2022; Mukai et al., 2014; Petley-Ragan et al., 2018; Zertani et al., 2019). One aim of this study was to gain new insights into whether a preweakening caused by a hydrogen influx is feasible and how it affects the subsequent inflow of an aqueous fluid.

Hydrous eclogite-facies phases, especially czs, are widely distributed throughout the entire cross section and are not limited to the shear zone (Figures 2d, 3i, 3j, 3k, and 3l). So, the bulk H_2O content increases toward the shear zone based on the increasing modal abundance of hydrous phases, assuming amph and czs to have 2 wt.% H_2O structurally bonded (e.g., Deer et al., 1997; Figure 2d, yellow curve). Initially, the H_2O uptake of the system is driven by the NAMs, which absorb almost 40% of the bulk H_2O (Figure 2d, red curve). However, during eclogitization, the OH incorporation of the system is mainly driven by the hydrous phases.

3. Numerical Model

A 1D mathematical shear zone model (Text ST1 in Supporting Information S1) was developed to investigate the transient viscosity changes during the fluid-induced shear zone formation. The hydration by aqueous fluid flow and by a diffusional hydrogen influx is described using diffusion equations. The effective rock viscosity is considered to be a function of the hydration. This model is based on those used in similar numerical studies

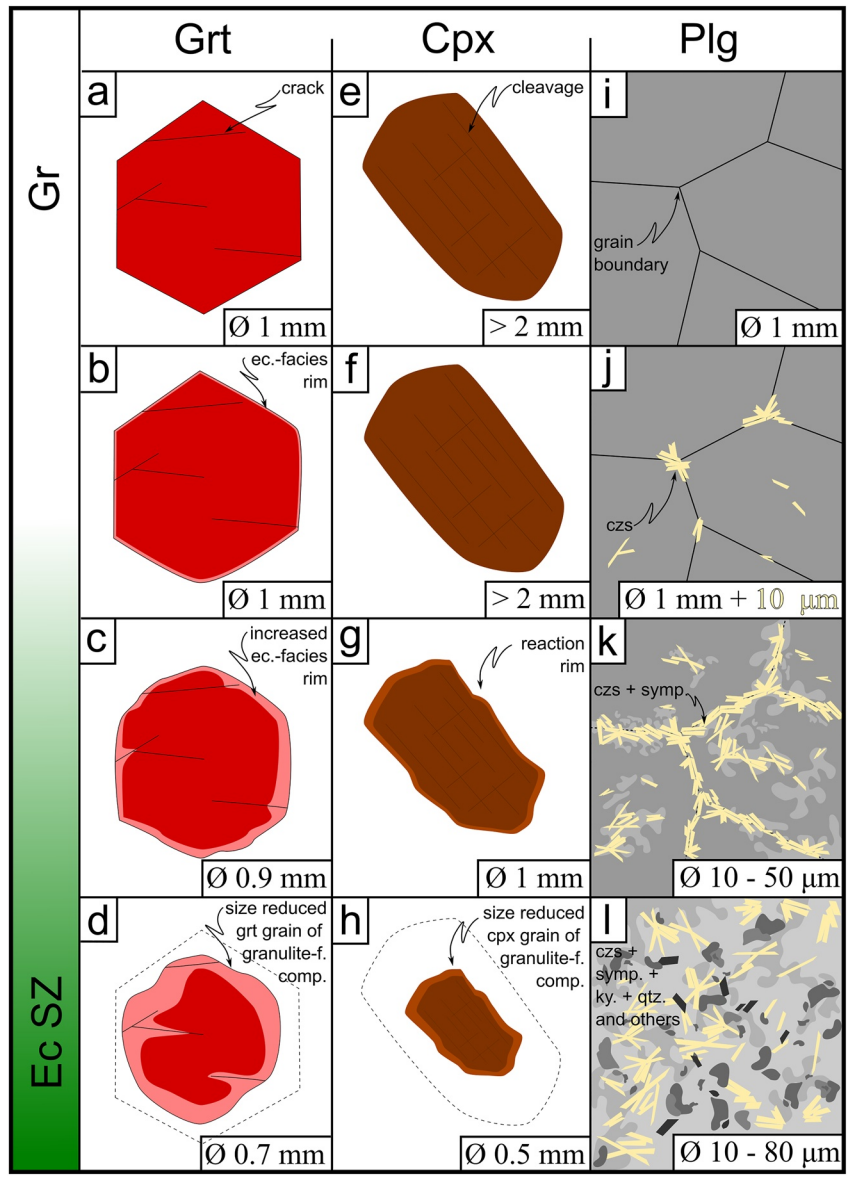

Figure 3. Sketch showing the textural and microstructural development for grt (a–d), cpx (e–h), and plg (i–l) from granulite (Gr) to the eclogite-facies shear zone (Ec SZ) including the grain size evolution based on dissolution-precipitation mechanisms. During eclogitization, grt develops an eclogite-facies Fe-rich rim (light red, b–d) while the grain size changes from approximately 1–0.7 mm, with a preserved granulite-facies composition within the core (d). Further, the isometric grain shape vanishes, and grt develops rims intergrown with omph at 120° angles at the scale of tens of microns (see d). The granulitic cpx (e) has a distinct cleavage and with decreasing distance to the shear zone and maintained granulite-facies composition, the grain size is reduced from >2 to ~0.5 mm (h). The plg undergoes the largest changes by complete separation of the phase in close vicinity and within the shear zone. First, czs needles form (j), often building symplectites with an albite-rich plg (k). Second, plg of granulite-facies composition is completely replaced by a symplectite consisting of czs, ky, qtz, and amph. This reaction causes a significant grain size minimization. Plg of granulitic composition does not indicate further deformation.

conducted by Bras et al. (2021) and Kaatz et al. (2021). The main elaborations of our model applied here are (a) the consideration of two simultaneous hydration processes, namely aqueous fluid flow and hydrogen diffusive influx, and (b) the comparison of the first-order spatial variation of the measured mineral phase abundance and the H_2O-content orthogonal to the shear zone, and of geometrical field data, being the shear zone thickness and the finite shear strain.

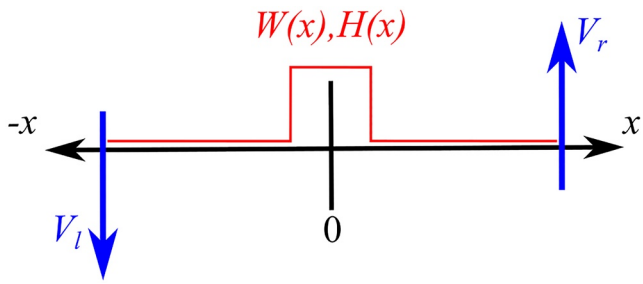

Figure 4. Model configuration for 1D sinistral simple shear deformation driven by boundary shear velocities V_l and V_r. Profiles of the initial distribution of the relative progress of eclogitization (W) and the relative amount of H_2O in the NAMs (H) are shown in red. Shearing and diffusion will be symmetric with respect to the center of the model at x-axis position = 0. Due to the applied symmetry, the center of the model will not be displaced in the direction of shearing.

3.1. The Mathematical Model

To investigate ductile deformation of a rock using numerical models requires a closed system of equations given by the concept of continuum mechanics (e.g., Pollard & Fletcher, 2005; Turcotte & Schubert, 2014). This set of equations contains (a) conservation equations, including the conservation of mass and of linear momentum (i.e., force balance), (b) constitutive equations, describing the rheological behavior of a material, for example, a linear viscous flow, and (c) kinematic equations, for example, characterizing the relation between velocity and strain rate. A 1D shear zone model (Figure 4) was used because it is simple and has a short computation time. The model configuration is dimensionless and scaling of the model results to natural conditions is discussed below.

For the model, viscous simple shear of an incompressible fluid in the absence of gravity is considered (Figure 4; e.g., Gerya, 2019; Pollard & Fletcher, 2005). The conservation of linear momentum for the considered 1D scenario is as follows:

$$0 = \frac{\partial \tau}{\partial x} \tag{1}$$

Here, x is the spatial coordinate and τ is the shear stress. The constitutive equation is (e.g., Gerya, 2019):

$$\tau = 2\eta_{eff}\,\dot{\varepsilon} \tag{2}$$

with η_{eff} being the effective viscosity of the material and $\dot{\varepsilon}$ the shear strain rate. The effective viscosity is a function of the hydration (see below). The shear strain rate is the spatial derivative of the shear velocity (V):

$$\dot{\varepsilon} = \frac{\partial V}{\partial x} \tag{3}$$

Hydration is described by a diffusion equation (e.g., Lasaga, 1998) that mimics the inflow of H_2O (W) or diffusion of hydrogen (H). For the H_2O inflow, the equation is as follows:

$$\frac{\partial W}{\partial t} = \frac{\partial}{\partial x}\left(D_w \frac{\partial W}{\partial x}\right) \tag{4}$$

W quantifies the relative progress of eclogitization. $W = 1$ for 100% eclogite-facies mineral phases, and $W = 0$ for dry granulite mineral assemblage. D_W represents the effective diffusivity. The same equation is used for the diffusional hydrogen influx, but W is replaced by H and D_W by D_H. H quantifies the relative amount of H_2O in the NAMs, representing the uptake of hydrogen. Hence, $H = 0$ for dry granulite, and $H = 1$ for reequilibrated eclogite, assuming maximum H_2O content within the shear zone.

The diffusivity of H_2O and hydrogen can be constant or variable. For a spatially and temporally variable diffusivity, it is assumed that the diffusivity is a nonlinear function of W or H. For diffusion of W, the following diffusivity is used:

$$D_{W\,\mathrm{non-linear}} = D_W \left[\frac{1+a}{W+a}\right]^b \tag{5}$$

with a and b being fitting parameters, where a defines how much the diffusivity changes between 0 and 1, and b specifies the variation of D_W based on the amount W. The variable diffusivity defined for the hydration of the NAMs, D_H, is based on H, and is described as given in Equation 5 but for different values of a and b.

Three end-member viscosities are considered in the model: The dry granulite viscosity $\eta 1$, the eclogite viscosity $\eta 2$, and the viscosity for fully hydrated granulite $\eta 3$ (Table 1). Two different hydration scenarios are modeled: single hydration, modeling only the diffusive-type inflow of H_2O, and double hydration, modeling the simultaneous diffusion-type inflow of H_2O and hydrogen influx. For single hydration, the effective viscosity, η_{eff}, is a mixture of $\eta 1$ and $\eta 2$, and the mixing is controlled by the value of W. The so-called Minimized Power Geometric

Table 1
Abbreviations Used in the Study

Explanation	Abbreviation	Units
Effective granulite viscosity	$\eta 1$	Pa·s
Effective eclogite viscosity	$\eta 2$	Pa·s
Effective viscosity of hydrated granulite	$\eta 3$	Pa·s
Aqueous H_2O inflow (eclogite-facies phase abundance)	W	vol.%
Hydrogen influx (OH incorporation in NAMs)	H	µg/g
Diffusivity of H_2O	D_W	m^2/s
Diffusivity of hydrogen	D_H	m^2/s
Displacement	U	m
Distance	X	m
Half of the shear zone thickness	k	m

(MPG) mixing model for viscously deforming polyphase rock (Huet et al., 2014) is applied to calculate the value of η_{eff} as function of $\eta 1$, $\eta 2$, and W. This mixing model was also applied to eclogite shear zones in granulite by Bras et al. (2021). For double hydration, first an effective viscosity for "hydrated" granulite is calculated from the values of $\eta 1$, $\eta 3$, and H using the MPG mixing model. Then, the value of η_{eff} is calculated from the effective viscosity of "hydrated" granulite, $\eta 2$, and W.

The system of equations described above is solved iteratively using a modified Richardson method, as described by Halter et al. (2022).

3.1.1. Boundary and Initial Conditions

The applied dimensionless boundary shear velocities are fixed, being 0.5 at right and −0.5 at the left of the model boundary, and 0 at the initial conditions inside the model (Figure 4). Therefore, during the simulations, the right model half will move upward, and the left model half will move downward, while the center of the model will exhibit zero velocities and, hence, zero displacement. Because of this symmetry of the shear zone model, we will display only the results for the right model half. Additionally, W and H are fixed to 1 for a restricted area of three grid points in the middle of the shear zone model, representing the eclogite-facies shear zone, and are fixed to 0 at the model boundaries. The model length was chosen to be large enough so that the diffusion did not reach the model boundaries at the end of the simulations. The finite shear strain value of 1 of the modeled shear zone, at which the simulation is stopped, is based on displacement calculations for a set of natural shear zones described in Kaatz et al. (2021).

For a first simulation, the following values were used: (a) granulite viscosity $\eta 1 = 1$, (b) viscosity ratios ($\eta 2/\eta 1$) or ($\eta 3/\eta 2$) = 10, (c) $D_W = 10$, and (d) diffusivity ratio (D_H/D_W) = 2.

3.2. Natural Data for Comparison With the Model Results

To compare changes within the mineral assemblage of the transforming rock and its petrophysical properties, the raw data indicating the fast hydrogen influx (incorporated OH-groups in NAMs, calculated to an H_2O content, Table ST2 in Supporting Information S1) and the slower inflow of the aqueous fluid (eclogite-facies phases modal abundance, Table ST3 in Supporting Information S1) is normalized (Figure 5). Here, normalization means that all values on the y-axis were divided by the maximum value of the specific data set, for example, H0 for the maximum H_2O content, resulting in a maximum value of 1 for all data sets, cf. y-axis Figures 5a–5d. The distance orthogonal across the shear zone (x-axis) was normalized (i.e., divided) by half of the modeled final shear zone thickness (k) to show the diffusion from the shear zone center into the granulitic wall rock because, for example, H_2O-contents are at maximum value within the shear zone center. For example, for a natural shear zone thickness of 2 cm (X/k []), the dimensionless X/k []-value of 2 on the x-axis corresponds to 2 cm (2 cm/1 cm = 2). This normalization simplifies the comparison between model results and natural data because specific dimensions are absent, and the profiles have the same starting point at both axes.

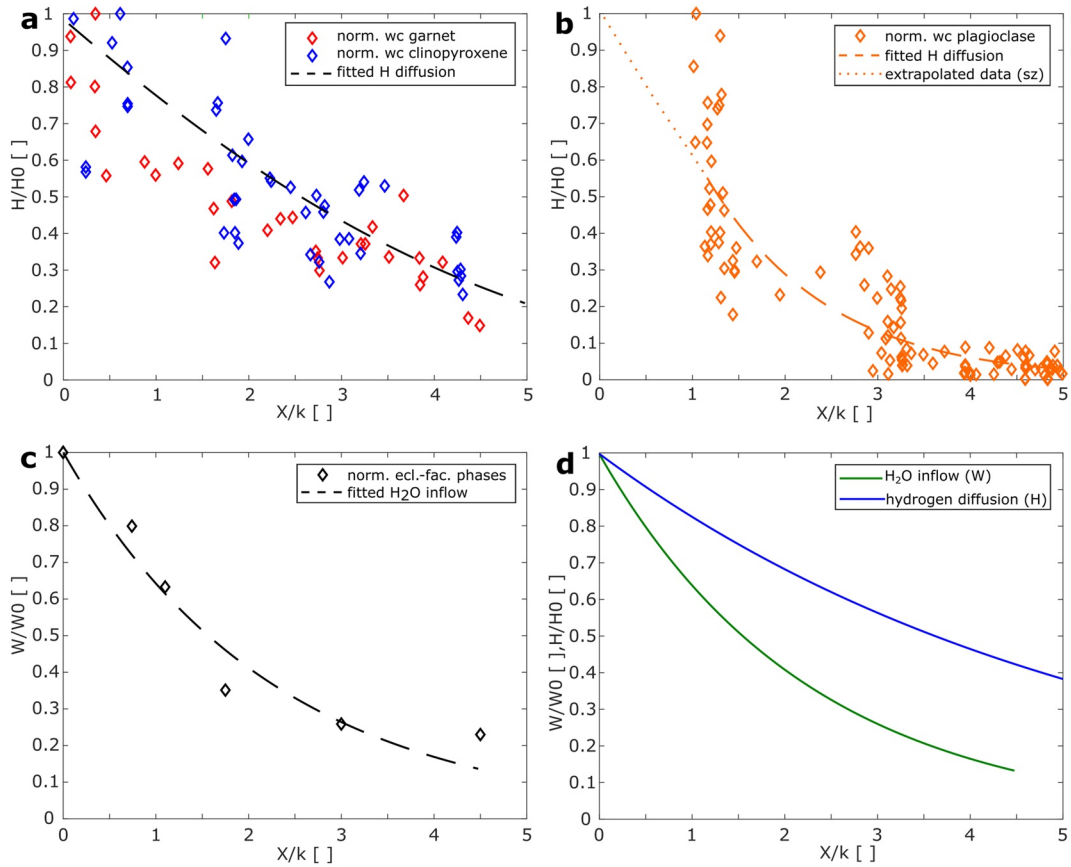

Figure 5. (a) Normalized H_2O content data (*H/H0 [ ]*) for garnet (red) and clinopyroxene (blue). One data point represents the average H_2O content measurements of one grain core (granulite-facies composition), which is fitted to a curve (black line), illustrating the hydrogen influx. (b) Normalized H_2O content data (*H/H0 [ ]*) for plagioclase (orange diamonds), representing the average core H_2O content. No plagioclase of pristine granulite composition is left next to the shear zone, causing a data gap between *x*-axis = 0 and *x*-axis = 1. The dashed fitted line indicates the hydrogen influx, while the dotted line is an extrapolation toward the shear zone. (c) Plotted variation of eclogite-facies phase abundance (black diamonds), where one point represents data of one phase map. The fitted curve illustrates the inflow of an aqueous fluid (*W*, dashed black line). (d) Comparison of both profiles, fast diffusional hydrogen influx (blue line) and slower inflow of H_2O (green line) along the normalized distance (*X/k [ ]*).

The H_2O contents measured within the NAMs of granulite-facies composition were plotted as normalized data (maximum value = 1) for grt (red), cpx (blue) in Figure 5a, and plg (orange) in Figure 5b. Here, each data point mimics one grain. Plotting grt and cpx and interpolating the data points resulted in a smooth profile (dashed line, Figure 5a) from the shear zone center (*X/k [ ]* = 0) to the granulite wall rock (*X/k [ ]* = 5). The plg H_2O content was plotted separately (Figure 5b). Due to phase separation, the granulite-facies plg in close vicinity to the shear zone was either too small to be measured with the FTIR or no reliable signal was detected and hence not used for further investigation. Therefore, the data were extrapolated (dotted orange line in Figure 5b) from the fitted H_2O content profile (dashed orange line in Figure 5b) to get a continuous profile as observed for grt and cpx (cf. Figure 5a). All continuous H_2O content profiles (grt, cpx, and plg) were finally combined into a bulk profile (Figure 5d blue line).

The eclogite-facies phase abundance is illustrated in Figure 5c (black dashed line), indicating an increasing abundance of eclogite-facies phases toward the shear zone. The phase abundances are based on several phase maps laterally distributed throughout the sample (Kaatz et al., 2022).

Figure 5d shows a comparison of both profiles: the bulk H_2O content variation in NAMs (blue line, based on the modal abundance of grt, cpx, and plg), implying a diffusional hydrogen influx, and the variation in eclogite-facies phase abundance (green line), indicating the inflow of an aqueous fluid. The two profiles imply that the hydrogen

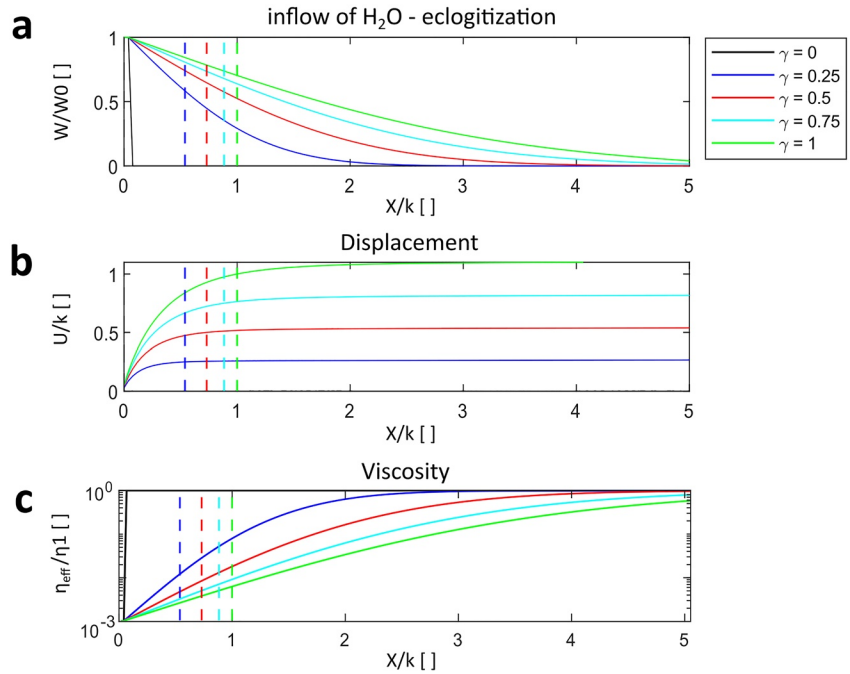

Figure 6. Evolution of the normalized eclogitization progress, *W/W0 [ ]* (a), representing H_2O inflow, (b) of total shear displacement normalized by half of the shear zone thickness, *U/k [ ]*, and (c) of the effective viscosity normalized by the viscosity corresponding to $W = 0$, $\eta_{eff}/\eta 1$ *[ ]* (i.e., dry granulite viscosity). Three profiles of *W/W0 [ ]*, *U/k [ ]* and $\eta_{eff}/\eta 1$ *[ ]* are displayed for five different shear strains between $\gamma = 0$ and $\gamma = 1$, including the shear zone thickness at given strain steps (dashed lines). The diffusivity D_w is constant. The *x*-axis shows the distance orthogonal to the shear zone, normalized by half of the final shear zone thickness, *X/k [ ]*. The *x*-axis position = 0 corresponds to the shear zone center.

influx progressed further into the wall rock than the H_2O and, hence, was faster than the aqueous fluid. The profiles shown in Figure 5d were used as representative natural profiles when comparing with the results of the numerical simulations.

4. Results

Two types of simulations were performed. First, single hydration of only H_2O inflow was modeled with a diffusion equation during shear zone formation. For this type of simulation, a first systematic series of simulations with different eclogite viscosities and different constant diffusivities was performed. The simulation results were compared with the natural data, and the best fitting values of eclogite viscosity and diffusivity were determined. For the single hydration simulations, a second systematic series was performed for which the diffusivity varied and depended on the amount of H_2O, *W* (see Equation 5).

For the second type of simulation, with double hydration, two diffusion-type hydration processes are considered that mimic the simultaneous inflow of H_2O and the hydrogen influx.

4.1. Single Hydration: Fitting the Inflow of H_2O—*W*—Eclogitization

4.1.1. Constant D_W

Figure 6 shows representative results for a 1D evolution of the H_2O inflow with constant D_W. After a maximum shear strain of 1 was reached, the simulation stopped. For five different shear strains, the evolution of the associated normalized displacement (*U/k [ ]*, Figure 6b) and the normalized effective viscosity ($\eta_{eff}/\eta 1$ *[ ]*, Figure 6c) is given. Both values depend on the evolution of the strain as well as the shear zone thickness. The shear zone thickness is defined by the shear strain profile across the model. Areas where the shear strain is higher than the mean shear strain of the system were defined to belong to the shear zone. One could use different criteria to define the shear zone thickness, but we need to apply one specific criterion to track the shear zone evolution

during the simulations. At the starting point, the shear zone center and rim are located at position 0 on the *x*-axis (Figure 6). The displacement is based on the strain propagation, hence the shear zone thickness over time, and was cumulatively added after each time step, resulting in the total displacement value. We display only the right-hand side of the model in Figure 6 (for positive *x*-values in Figure 4) and, hence, the normalized displacement, *U/k []*, is the total displacement in the right model half divided by half of the final, total shear zone thickness (*k*). Hence, the final *U/k []* = γ, for the dimensionless model configuration.

The displacement and η_{eff} evolution are based on the diffusion of *W* (Figure 6a). At initial conditions, $\gamma = 0$, no strain is present, no shearing has occurred, and *W/W*0 *[]* = 1 within the shear zone (0 on the *x*-axis). Consequently, at the beginning, the displacement *U/k []* = 0 within this area (Figure 6b). If shearing is applied and the *W* profile diffuses, *U/k []* evolves and increases to a maximum value of 1 ($\gamma = 1$), implying shear zone widening based on the distribution of W and shearing. *U/k []* is cumulatively added after each time step, causing a consistent starting point at *x*-axis position = 0, being the center of the shear zone, for each γ. $\eta_{eff}/\eta 1$ *[]* is low within the shear zone (Figure 6c) because *W/W*0 *[]* = 1 within the same area. Consequently, both values create step-like profiles from shear zone to granulite for the initial situation at $\gamma = 0$ (Figure 6a). As soon as *W* diffuses over time, η_{eff} adjusts as well (cf. Figures 6a and 6c).

4.1.2. Variable D_W

A nonlinear diffusion with spatial and temporal variation of D_W according to Equation 5 enables an adjustment of the shape of the modeled *W*-profile. Figure 7a displays representative results of the nonlinear *W* inflow. Initial conditions are the same for constant D_W (cf. Figures 6 and 7), but at $\gamma = 0.25$ the gradient of *W/W*0 *[]* is higher (blue line Figure 7a) compared to a constant D_W (Figure 6a), causing a steeper *W*-profile. However, *W/W*0 *[]* and $\eta_{eff}/\eta 1$ *[]* are still interdependent, and if *W/W*0 *[]* diffuses then $\eta_{eff}/\eta 1$ *[]* changes as well. The normalized displacement *U/k []* is given in Figure 7b, which increases over time with increasing *W* distribution. Compared to Figure 6b, the displacement steps decrease with increasing shear strain but are not constant. The applied values of D_W decrease toward the shear zone (Figure 7d).

4.1.3. Systematics

More than 100 simulations were performed with various values for the dimensionless D_W (5–60) and the dimensionless $\eta 2$ (10^{-5}–10^{-2}) to find the smallest misfit between the normalized field-derived phase abundance and H_2O-content profiles and the modeled diffusion profiles (Figure 8). The phase abundance and H_2O-content values were interpolated onto the grid points of the numerical model. Thereby, the observed and modeled values for *W* and *H* could be compared at every numerical grid point. The relative difference between the modeled and measured value was calculated at every grid point and divided by the measured, field-derived value. The arithmetic average of all misfits along a profile, multiplied by 100, was then considered as the average misfit in percentage for each simulation.

The misfit plot in Figure 8a shows that the required value of $\eta 2$ to best fit the phase abundance data increases with increasing values of D_W. Using a constant D_W, the minimum misfit reached was <10% for $\eta 2 = 10^{-3}$ and $D_W = 50$. As shown in Figure 8b, the normalized *W* model profile never perfectly fit the phase abundance profile (*W*-data).

To improve the fit that was obtained with constant D_W, more than 100 simulations with a variable D_W and variable $\eta 2$ were performed. Results show an almost perfect fit (Figure 8d) with values $a = 0.01$ and $b = 0.5$ (see Equation 5) with a minimum misfit <2% (Figure 8c) at values of $\eta 2 = 2.5 \times 10^{-4}$ and $D_W = 20$. However, as described for Figure 7d, the D_W decreased from the granulite toward the shear zone, which is difficult to justify and is discussed below.

4.1.4. Potential Flattening of the Shear Zone

Another way to fit the *W* profile is to assume that the shear zone also exhibited a component of shear zone-orthogonal flattening, that is, a pure shear thinning component in addition to the simple shear component. In the 1D shear zone model presented here, no simultaneous simple shearing and pure shear flattening can be simulated. Therefore, a pure shear shortening was applied to the final *W* profile, which was obtained by simple shearing only. The aim of applying such an a posteriori pure shear flattening was to test whether such flattening could indeed decrease the misfit between the modeled and natural *W* profiles, if D_W is kept constant.

In the case of a 1D simulation, flattening causes a shortening of the material in the *x*-direction. In the model, the flattening was applied between coordinates 0 and 2 on the *x*-axis to guarantee for the conversion of natural observations that the pure shear flattening component was mainly present within and in close vicinity to the shear zone.

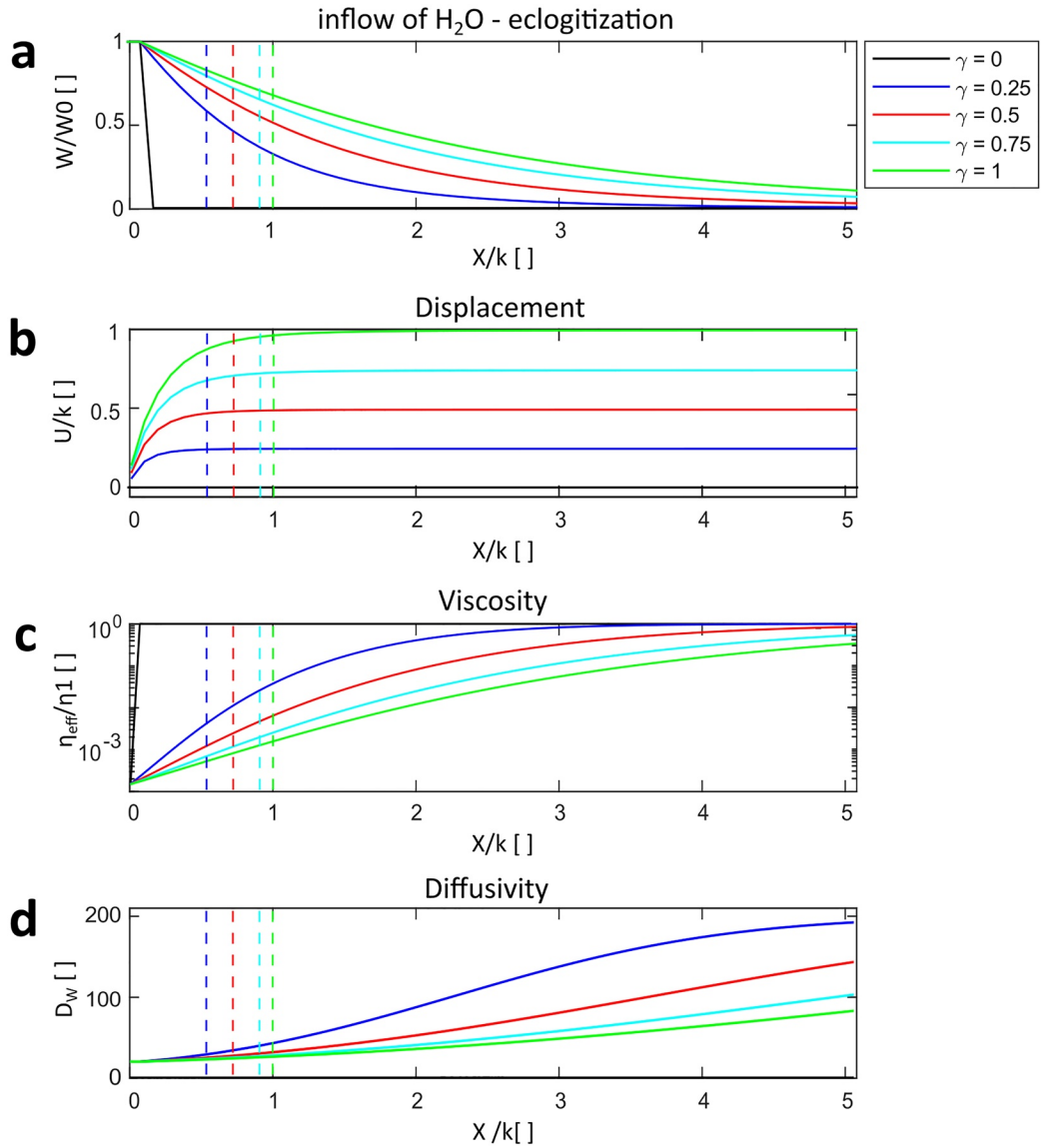

Figure 7. Nonlinear H_2O inflow indicating the (a) normalized eclogite-facies phase abundance *W/W0 [ ]*, (b) shows the normalized displacement adjusted by half of the shear zone width, *U/k [ ]*, (c) the dimensionless effective viscosity $\eta_{eff}/\eta 1$ *[ ]*, and (d) the variable diffusivity D_W for five steps of shear strain from $\gamma = 0$ to $\gamma = 1$, including the shear zone thickness at given strain steps (dashed lines). *X/k [ ]* is the dimensionless distance divided by half the shear zone width, where 0 corresponds to the shear zone center.

Results show that when a 30% flattening was applied, an almost perfect fit was achieved (Figure 8e, yellow line). To find the best fit including pure shear flattening, results of the previous systematic simulations were used, and flattening was applied manually. The modeled and flattened profiles having the lowest percentage of flattening but the highest overlap with the *W* profile were achieved with the following parameters: $\eta 2 = 10^{-4}$, $D_W = 41$, and 30% flattening. These parameters are slightly different than those used in Figure 8b profile, without flattening.

4.2. Double Hydration: Fitting the Inflow of H_2O (*W*) and Hydrogen Influx (*H*, Hydration of NAMs)

4.2.1. Constant D_W and D_H

In a second series of simulations, those including double hydration, the hydrogen influx was considered by adding a second diffusion model to the shear zone model. The natural data indicate that the bulk hydrogen influx progressed further into the granulite (Figure 5d). To find the best fit diffusivity ratio (D_H/D_W) and viscosity ratio ($\eta 3/\eta 2$), more than 100 simulations were performed. Both hydration processes were modeled with diffusion equa-

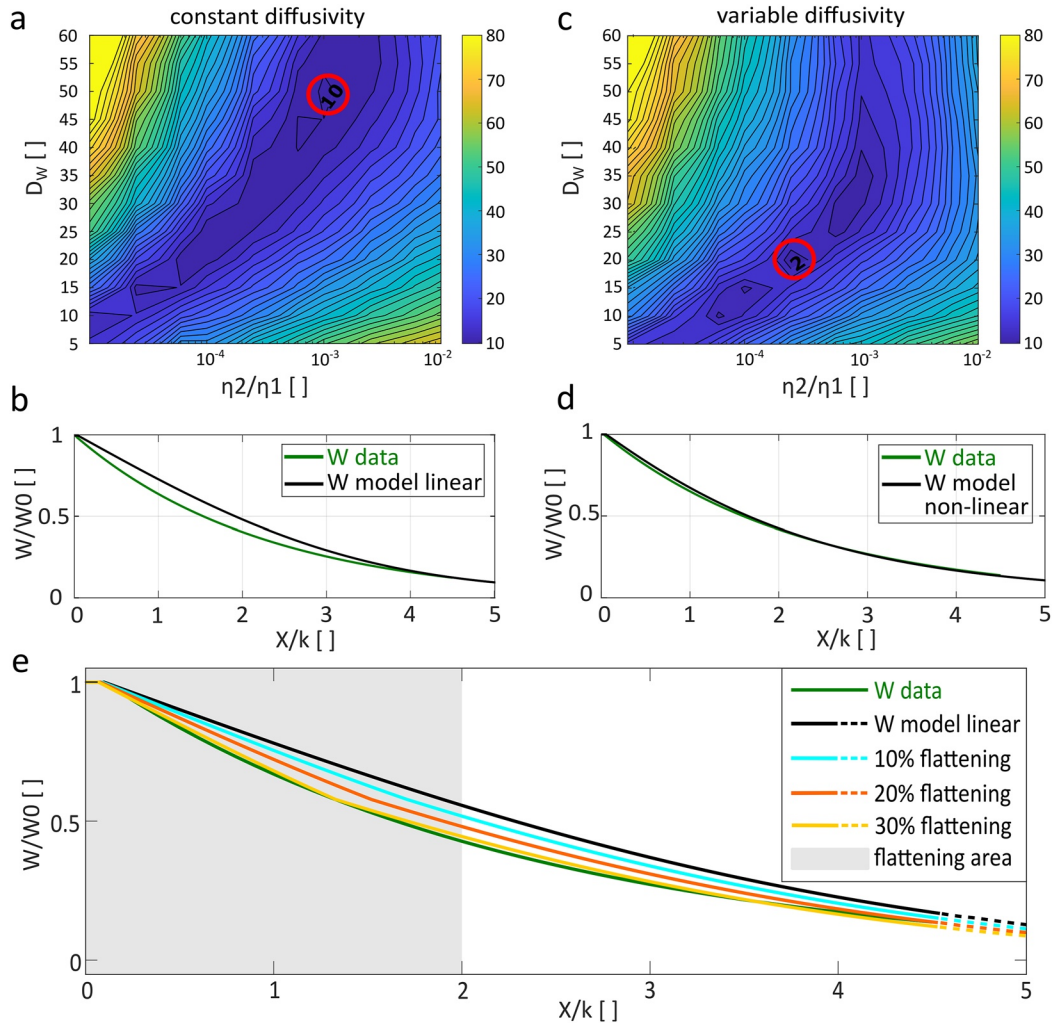

Figure 8. Best fit results of the inflow of H_2O, *W/W0 [ ]*, with constant diffusivity (a, b) and variable diffusivity (c, d). Contour-plots in (a) and (c) show nondimensional diffusivities, $D_{W,}$ versus normalized eclogite viscosities, $\eta 2/\eta 1$ *[ ]*, whereby the color bars display the misfit of the field-derived and the simulated *W*-profiles in percentage. The minimum misfit is <10% with a constant D_W and <2% with a variable D_W. The associated best fit profiles are displayed in (b) and (d) having the amount of *W* on the *y*-axis, where 1 corresponds to 100% eclogite-facies phase, versus the normalized distance, *X/k [ ]*, on the *x*-axis. (d) Results of linear inflow of H_2O including 10%–30% pure shear flattening in the vicinity of the shear zone (<2 *X/k [ ]*).

tions with constant D_W and D_H. Figure 9a shows the best fit results, which have an average misfit of ∼10% for *W* and <4% for *H*, with $D_W = 35$, $D_H = \sim 133$, which is ∼3.8 times higher than D_W, $\eta 2 = 10^{-4}$, and $\eta 3 = 10^{-2}$. Best fit including flattening for both hydration processes between coordinates 0 and 2 on the *x*-axis (Figure 9b) resulted in $D_W = 50$, $D_H = \sim 190$ (4 times higher than D_W), $\eta 2 = 10^{-4}$, $\eta 3 = 10^{-2}$, and 30% flattening.

5. Discussion

The most striking result of this study is that diffusive hydrogen influx, in addition to aqueous fluid inflow, temporally changes the effective diffusivities and effective viscosities, while reequilibration reactions occur. Thereby, the phase abundance and H_2O-content data can be reproduced with a relatively simple 1D diffusion model.

5.1. Justification for the Model Setup

Field evidence and measured petrological data showed that the fluid influx, metamorphic reactions, and deformation occurred contemporaneously, developing at different lengths and probable time scales (e.g., Kaatz et al., 2022). The shape of the averaged H_2O-content profile and phase abundance profile (Figure 5d) justifies the assumption that both

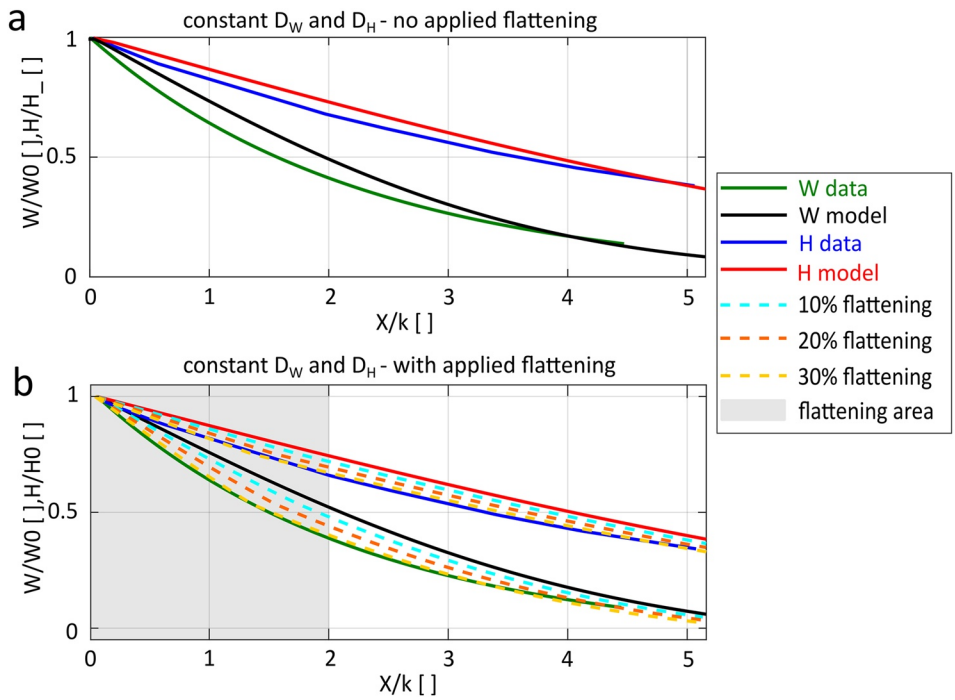

Figure 9. Double hydration due to H_2O inflow (*W/W0 [ ]*) and diffusional hydrogen influx (*H/H0 [ ]*) with constant D_W and D_H, respectively. Best fit results are given for (a) hydration profiles without flattening, and (b) with an applied flattening (10%–30%). The normalized amounts of *W* and *H* are displayed on the *y*-axis, where 1 corresponds to 100% eclogite-facies phase abundance for *W/W0 [ ]* and 100% H_2O-content in the NAMs for *H/H0 [ ]*. On the *x*-axis, the nondimensional distance, *X/k [ ]*, is given. The lowest misfit is generated with a 30% flattening for $D_W = 50$, $D_H = \sim 190$, $\eta 2 = 10^{-4}$, and $\eta 3 = 10^{-2}$.

hydration processes feature overall diffusion-type processes. Accordingly, both hydration processes are approximated by and, hence, modeled with a simple diffusion equation. Thus, the applied diffusion model does not model the exact hydration processes but rather mimics all processes involved and resulted in the spatial and temporal variation of the H_2O inflow and hydrogen influx (Figure 5d). During natural hydration, physical-chemical processes such as the changing kinetics of mineral reactions, grain size reductions, dissolution-transport precipitation, mass transfer, formation of transient porosity, and permeability occur and are certainly important. However, they are not explicitly considered in our model. The applied simple diffusion model represents an approximation of the combined effects of all such physical-chemical processes at the moment of metamorphic reequilibration from granulite to eclogite.

5.1.1. Local Thermodynamic Equilibrium

A recent study by Zertani et al. (2022) utilized the static eclogite-facies overprint observed on Holsnøy to identify how hydration and eclogitization reactions are thermodynamically linked. They concluded that the reactive fluid flow leading to eclogitization is guided by gains in Gibbs free energy at grain boundaries, such that mineral reactions producing the greatest energy drop occur first. This implies that the eclogitization occurring far from equilibrium is not kinetically delayed (Zertani et al., 2022), and hence, approximating instantaneous mineral reactions is a valid assumption.

5.1.2. Diffusivity and Porosity

The plg-plg reactions initiate a grain size minimization of the granulite matrix of about three orders of magnitude (Figure 3), accompanied by a densification and, hence, the local formation of porosity (e.g., Zertani et al., 2022); a transient porosity increase is a common feature of fluid-mediated rock transformation (e.g., Beinlich et al., 2020; John et al., 2012; Putnis, 2021). Plümper et al. (2017) showed that the plg breakdown creates nanopores, which support electrokinetic fluid and mass transport through the system without the need for an additional dynamic driving force such as high fluid pressure gradients. Additionally, Fusseis et al. (2009) suggested that within shear zones, fluids might be advectively transported via newly created pores during deformation-related dissolution-precipitation reactions, initiating a self-generated granular fluid pump. For the analyzed sample, the

determined remaining porosity after metamorphism and deformation shows a gradient in which, at a pressure of 2.0 GPa, the eclogite-facies shear zone has the highest porosity with 1.8×10^{-2}, the transition zone has a moderate porosity with 1.2×10^{-2}, and the original granulite has the lowest porosity with 5.5×10^{-3} (raw data in Supporting Information S1—Table ST4). Although all observations and processes described above should result in an increase in the effective diffusivity of the infiltrating media from the granulite toward and into the shear zone, a decrease in the D_W and D_H in the model with variable diffusivity (Figure 7d) is found instead. This behavior is counterintuitive with respect to the measured porosity and the observed granulite to eclogite transformation. Consequently, the fitted model in which a nonlinear diffusivity was applied, which created increasing diffusivities from eclogite to granulite, is physically not feasible, although it produced a very good fit (Figure 8d).

5.1.3. Diffusivity and Mechanical Flattening

An additional a posteriori mechanical deformation was applied to the diffusion model based on previous findings, suggesting that a pure shear flattening component is frequently observed for natural shear zones. Typically, they feature a pure shear flattening of 10%–40% within and close to the shear zone (e.g., review of Fossen & Cavalcante, 2017, their Figure 9). If this is also true for the analyzed shear zone, the phase abundance and H_2O-content data presented in Figure 5 would already include a pure shear component, hence, a flattening of the rock. However, our simple 1D numerical shear zone model only mimics the diffusional transport into the system during simple shear. Therefore, a pure shear component was applied during post processing within a restricted area between $X/k\,[\,] = 0$ and 2 (gray area, Figure 9b). This is suitable for the investigated profiles because (a) bending of the granulite foliation is detectable throughout this area and (b) granulitic plg grains already reacted, leading to a very fine-grained matrix. These microstructures are probably related to a kind of ductile deformation beside the fluid-assisted metamorphic reequilibration. However, for the best fit, both final modeled hydration profiles showed no changes in either the viscosity values (still $\eta 2 = 10^{-4}$, $\eta 3 = 10^{-2}$) or the diffusivity ratio ($D_H = -4 \times D_W$) when flattening was applied, which, consequently, supports the assumption of a pure shear flattening component.

5.2. Parameterization

The set of equations used in this study was solved in a nondimensional form. To understand the meaning of the model results, the strain rate $\dot{\varepsilon}$, shear stress τ, viscosities $\eta 1$–$\eta 3$, diffusivities D_W and D_H, and duration t were recalculated assuming typical subduction zone velocities Vc. The recalculations were based on the best fit results for the model with diffusional hydrogen influx and H_2O inflow with constant diffusivities and 30% pure shear flattening, as presented in Figure 9b, for a 2 cm-wide shear zone. This shear zone width agrees with the analyzed shear zone profile. The simulations gave the following consistent results: (a) a viscosity ratio $\eta 1/\eta 2$ of 10^4 and $\eta 1/\eta 3$ of 10^2 and (b) $D_H/D_W = \sim 4$. The compilated results shown in Figure 10 indicate a most likely range for all parameters, while the fluid-assisted reequilibration reactions occur.

5.2.1. Viscosities $\eta 1$–$\eta 3$

Previous studies used a minimum effective viscosity for the dry granulites on Holsnøy at given P-T conditions of 10^{22} Pa·s (e.g., Bras et al., 2021; Labrousse et al., 2010), which was derived from an approximation for dry anorthite (e.g., Rybacki & Dresen, 2000). Using the modeled viscosity ratios, this results in a natural granulite viscosity of 10^{22} Pa·s, a temporary effective eclogite viscosity during the transformation of 10^{18} Pa·s, and an effective viscosity for the hydrated granulite of 10^{20} Pa·s during reequilibration and shearing. It should be noted here that the weakening is considered to be a transient effect and that the full rock strength of, for example, eclogite is suggested to reestablish once the reaction has gone to completion.

Using field-based paleostress data of various mylonitic shear zones observed in lower crustal rocks, Bürgmann and Dresen (2008) concluded that viscosity differences of up to three orders of magnitude between the rigid wall rock and weaker shear zone are required for ductile deformation by supposing constant far-field stress. These findings coincide with the field-based results presented here, which are also consistent with the viscosity calculations of Bras et al. (2021).

5.2.2. Rheological Behavior

One of the outcomes of the modeling was that the rheological behavior of the system changes when a diffusional hydrogen influx is applied along with the inflow of an aqueous fluid (Figure 8 vs. Figure 9). If hydration only occurs by aqueous fluid inflow, the resulting viscosity ratio $\eta 1/\eta 2$ (dry granulite/eclogite) is 10^3, whereas when an additional hydrogen influx is considered, the transient weakening effect is more enhanced, $\eta 1/\eta 2 = 10^4$. This result

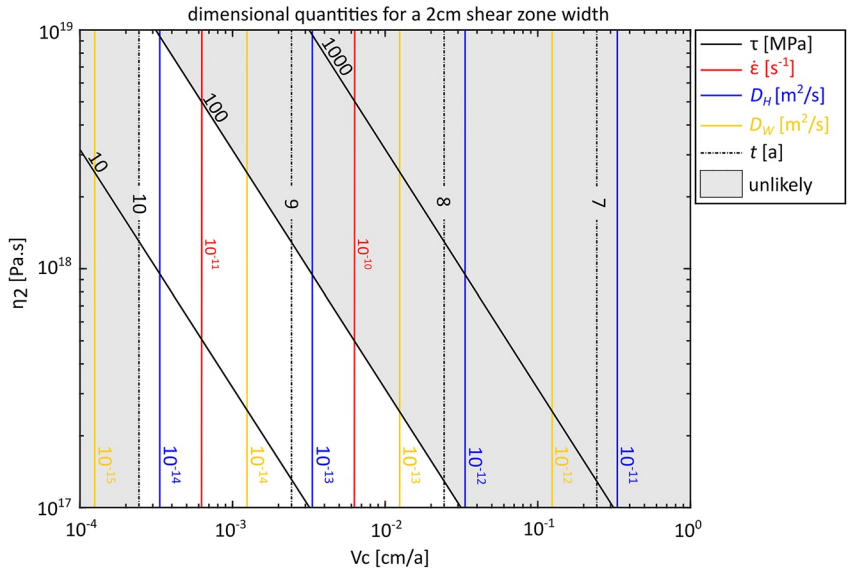

Figure 10. Scaling of the nondimensional results to dimensional quantities using specific values for the shear velocities (*Vc*, horizontal axis), the eclogite viscosity ($\eta 2$, vertical axis) and a shear zone thickness of 2 cm. Contour lines indicate shear stress (τ), strain rate ($\dot{\varepsilon}$), hydrogen diffusivity (D_H), aqueous fluid diffusivity (D_W), and time (t). Natural shear stresses of >100 MPa and a time estimate >10 are unlikely and, consequently, reflect the limit of reliable associated quantities calculated here.

suggests that hydrogen incorporation influences the effective viscosity of the affected rocks. It is well known that significant rheological changes occur due to metamorphic reequilibration by fluid-induced dissolution-precipitation processes and transient hydration of the wall rock (e.g., Gueydan et al., 2003; Handy, 1989; Plümper et al., 2017).

The transient weakening and increased deformability of the system is facilitated by mechanisms such as dissolution-precipitation creep, dislocation creep, grain-boundary sliding, and diffusion creep because these processes mainly control the evolution of the rock strength (e.g., Brodie & Rutter, 1987; Marti et al., 2018; Oliot et al., 2010; Stünitz et al., 2020). Plagioclase in particular plays a major role in the localized weakening and deformation, since it is the most abundant mineral occurring in the crust, for example, in the Holsnøy granulite it constitutes ~60 vol.% (e.g., Altenberger & Wilhelm, 2000; Wain et al., 2001; Wayte et al., 1989). The plg breakdown causes a reaction softening (e.g., Rubie, 1983), which facilitates ductile deformation because recrystallized grain sizes are reduced (e.g., FitzGerald & Stünitz, 1993; Giuntoli et al., 2018; Tullis & Yund, 1985; Wehrens et al., 2017). Nevertheless, it is still a matter of debate which mechanisms weaken plg and whether the incorporation of hydrogen can initiate a weakening.

Potentially, plg weakening is driven by dissolution-precipitation along the grain boundaries, as observed in qtz (e.g., Stünitz et al., 2017). Indeed, on Holsnøy, plg grain boundaries are highly reactive, and the reequilibrated mineral assemblage is very fine-grained (Figure 3, e.g., Kaatz et al., 2022; Moore et al., 2019; Zertani et al., 2022). Additionally, immediate plg breakdown after limited hydrogen uptake was demonstrated by Kaatz et al. (2022), suggesting that the plg structure may become less stable after a certain level of OH incorporation due to a pervasive hydrogen influx. The plg weakening could occur similarly to the weakening of olivine, where hydrogen bonds to point defects within the crystal lattice, which promotes dislocation climb (e.g., Kohlstedt & Mackwell, 1998; Mackwell & Kohlstedt, 1990; Mackwell et al., 1985; Tielke et al., 2017), progressively weakens the minerals, and enhance its plasticity over time. Potentially more important is that the weak and probably unstable plg structure is expected to flow at very low stresses, as shown by Lasaga and Blum (1986). This may explain why the weakening affecting the rock seems to increase when hydration includes both an aqueous fluid inflow and hydrogen influx (see viscosity ratios above). Plagioclase does indeed contribute to the weakening. Consequently, deciphering the weakening mechanism initiated by hydrogen should be part of upcoming research, since the significance of plg for deformation of the deeply buried continental crust may still be underestimated.

5.2.3. Shear Stress τ, Velocities *Vc*, and Strain Rate $\dot{\varepsilon}$

Figure 10 displays the corresponding shear stress (MPa) for various $\eta 2$, resulting in a realistic range for $\eta 1$ from 10^{21} to 10^{23} Pa·s and values for *Vc* from 10^{-5} to 1 cm/a, which are used to calculate the shear strain rates for a

2 cm thick shear zone. The most probable shear stresses (<100 MPa) are generated if Vc is $<10^{-2}$ cm/a. The shear stress is based on the strain rate, $\dot{\varepsilon}$, which is a spatial derivative of Vc. If a Vc of $>10^{-2}$ cm/a is considered, the resulting $\dot{\varepsilon}$ reach values $>10^{-10}$ s^{-1}, which are rather unlikely (Figure 10). The strain rate was not implemented into the numerical simulation as a references value but was recalculated using the real shear zone width (in m) divided by the modeled shear zone width. Usually, strain rates used for similar shear zone models on Holsnøy are 10^{-14}–10^{-13} s^{-1} (e.g., Bras et al., 2021; Kaatz et al., 2021; Labrousse et al., 2010). Lower limits of typical strain rates for crustal rocks and eclogite-facies shear bands are 10^{-14} s^{-1} (e.g., Fagereng & Biggs, 2019), but can be as high as 10^{-13}–10^{-12} s^{-1} (e.g., Terry & Heidelbach, 2006), respectively.

Convergence rates at subduction zones vary between approximately 2 and 10 cm/a (e.g., Syracuse et al., 2010) and are <5 cm/a for continental collision zones (e.g., Guillot et al., 2003; Li, 2014). Eclogitization and shear zone formation on Holsnøy occurred at >80 km depth and produced a network of shear zones ranging from the cm to the km-scale, which are distributed over the region. Several authors have shown that strain is partitioned between shear zones, especially within large complex shear zone networks, which results in inhomogeneous deformation patterns (e.g., Carreras et al., 2013; Fossen & Cavalcante, 2017; Fusseis et al., 2006; Schrank et al., 2008; Wehrens et al., 2017). Hence, a velocity partitioning among single shear zones of a contemporaneously active and evolving shear zone network, such as the one on Holsnøy, should result in low values of local Vc for the individual shear zones. Using typical strain rates (10^{-14}–10^{-13} s^{-1}), and shear zone widths (~0.5 m) as published in previous studies (e.g., Bras et al., 2021; Labrousse et al., 2010), the calculated Vc may vary between 10^{-5} and 10^{-4} cm/a, which is in agreement with the presented results.

One final note about model-calculated shear stresses is that the shear stresses increase linearly with increasing strain rates because of the linear viscous flow law used in the numerical model. However, if a power-law flow law with a stress (or strain rate) dependent effective viscosity would have been applied, which is probably closer to reality but would have resulted in more complexity, the stress increase with increasing strain rate would be less.

5.2.4. Diffusivities D_W and D_H

The diffusivity for the aqueous fluid inflow, D_W, and the hydrogen influx, D_H, are also given in Figure 10 for various $\eta 2$, different Vc, and for a 2 cm-wide shear zone. If reasonable strain rates and shear stresses are applied ($Vc < 10^{-2}$ cm/a), D_W varies between 10^{-15} and 10^{-13} m^2/s, and D_H between 10^{-14} and 10^{-12} m^2/s. The differences between the two types of hydration are that (a) for the hydrogen influx, volume diffusion through the crystal lattice is accompanied by grain-boundary diffusion, whereas (b) for the aqueous fluid inflow, which delivers H_2O and additional hydrogen, diffusion is basically controlled by grain-boundary transport along already "hydrated" and equilibrating grain boundaries (e.g., Kaatz et al., 2022). Referring to the diffusional hydrogen influx first, Ingrin and Blanchard (2006) demonstrated that reliable diffusivities for the hydrogen uptake in granulite- and eclogite-facies minerals such as grt and cpx vary between 10^{-15} and 10^{-11} m^2/s for $T > 900$°C. Reynes et al. (2018) performed hydration experiments of grt at temperatures of 750°C and obtained diffusivities for hydrogen incorporation from 10^{-15} to 10^{-13} m^2/s. Additionally, the results of Dohmen and Milke (2010) were based on bulk diffusion modeling including volume and grain-boundary diffusion, and they found an effective total diffusivity of 10^{-12} m^2/s. Consequentially, the modeled D_H value agrees with the current knowledge.

The modeled effective D_W is one order of magnitude lower than D_H. The resulting value of $10^{-14\pm1}$ m^2/s is in agreement with previously estimated bulk diffusivities for the infiltration of aqueous fluid on Holsnøy when the applied strain rate is 10^{-13} s^{-1} (e.g., Bras et al., 2021; Kaatz et al., 2021; Malvoisin et al., 2020). However, the inflow of aqueous fluid is controlled by grain-boundary diffusion, which is, especially under fluid-saturated conditions and in reactive systems, very efficient, with diffusivities of 10^{-12} m^2/s, (e.g., Dohmen & Milke, 2010; Taetz et al., 2018). Dohmen and Milke (2010) concluded that typical diffusivity ratios of grain-boundary versus volume diffusion differ between 10^4 and 10^7, which suggests that the hydrogen influx is slowed down significantly by its volume diffusion component, resulting in rather similar bulk diffusivities of both hydration processes ($D_W = 10^{-14\pm1}$ m^2/s vs. $D_H = 10^{-13\pm1}$ m^2/s). Nevertheless, the model value for D_H is only one order of magnitude faster than D_W, and both agree with published values.

5.2.5. Time t, Duration of the Shear Deformation

The duration of shearing calculated here is based on Vc and the shear zone width (2 cm). Time estimates for the duration of metamorphic rock transformation and single shear zone formation are rare, as is the case for almost all rather short-lived geological processes (e.g., Beinlich et al., 2020). However, within the scope of a previous

study, Kaatz et al. (2022) estimated a duration of 2 years for the hydration of a single grt grain within the same investigated shear zone. This duration reflects the time the grt had to equilibrate with the elevated hydrogen concentration during the fluid-mediated shear zone formation. Using chronometric diffusion modeling, John et al. (2012), Taetz et al. (2018), and Beinlich et al. (2020) found that the lifetimes of metamorphic hydrothermal vein-wall rock systems were ~800 a, ~20 a and a few months, respectively, with reaction front propagation velocities ranging between a few cm/a and dm/a. Malvoisin et al. (2020) showed that fluid-induced densification reactions proceed on the order of weeks. Furthermore, heat flow modeling using Ar^{40}–Ar^{39} mineral data indicated that a heating of a 30-m granulite lens from 385°C to 526°C (by ~700°C hot fluid) might have occurred within ~10 years (e.g., Camacho et al., 2005). According to these previous studies, it seems that a duration of more than 10 years for the eclogitization and deformation of the 2 cm-wide shear zone studied here is rather unlikely. Hence, this is considered as another limiting factor for the recalculated results (Figure 10).

6. Conclusions

The presented results demonstrate that in addition to the inflow of aqueous fluid, an additional hydrogen influx affects the evolving rock strength while fluid infiltration, metamorphic reequilibration, and ductile deformation occur. Two contemporaneous hydration processes with different speeds and pervasivenesss, namely H_2O and hydrogen influx, were simulated using a simple 1D shear zone model. The results show that during reaction progress and shearing, the effective viscosity of the eclogite needs to be four orders of magnitude lower than the viscosity of the dry granulite to reproduce the analyzed H_2O-content and phase abundances of the sample. Further, the effective viscosity of hydrated granulite needs to be two orders of magnitude lower than the viscosity of the dry granulite, while reacting. The hydrogen influx slightly changes the effective diffusivities, where the diffusivity of hydrogen is approximately $10^{-13\pm1}$ m^2/s, and the aqueous fluid diffusivity is $10^{-14\pm1}$ m^2/s. Estimates for the duration of the hydration and shearing as well as constraints for the shear velocity are <10 years and $<10^{-2}$ cm/a, respectively.

Overall, this study shows how a simple numerical model, validated by constraints based on field data, can provide detailed information on the dynamic evolution of petrophysical parameters of deeply buried crustal rocks. Notably, the presented model describes how fluid inflow transiently modifies the rock strength of subducting continental crust.

Data Availability Statements

The data and numerical code used to produce the results presented in this study are available in the supplementary material and in the repository: https://doi.org/10.5281/zenodo.7734246, respectively.

Acknowledgments
This study was partially funded by the Deutsche Forschungsgemeinschaft (DFG) through a Grant by CRC 1114 "Scaling Cascades in Complex Systems," Project number 235221301, Project (C09)—"Dynamics of rock dehydration on multiple scales." This study was also supported by the University of Lausanne. The porosity measurements were conducted by the Core Laboratories in Huston, USA. We thank Philippe Yamato, Marie Baïsset, Erwan Bras and Loïc Labrousse for providing the viscosity mixing model they used in Bras et al. (2021). Open Access funding enabled and organized by Projekt DEAL.

References

Altenberger, U., & Wilhelm, S. (2000). Ductile deformation of K-feldspar in dry eclogite facies shear zones in the Bergen Arcs, Norway. *Tectonophysics*, *320*(2), 107–121. https://doi.org/10.1016/s0040-1951(00)00048-2

Andersen, T. B., Corfu, F., Labrousse, L., & Osmundsen, P.-T. (2012). Evidence for hyperextension along the pre-Caledonian margin of Baltica. *Journal of the Geological Society*, *169*(5), 601–612. https://doi.org/10.1144/0016-76492012-011

Andersen, T. B., Jamtveit, B., Dewey, J. F., & Swensson, E. (1991). Subduction and eduction of continental crust: Major mechanisms during continent-continent collision and orogenic extensional collapse, a model based on the south Norwegian Caledonides. *Terra Nova*, *3*(3), 303–310. https://doi.org/10.1111/j.1365-3121.1991.tb00148.x

Austrheim, H. (1987). Eclogitization of lower crustal granulites by fluid migration through shear zones. *Earth and Planetary Science Letters*, *81*(2–3), 221–232. https://doi.org/10.1016/0012-821x(87)90158-0

Austrheim, H., & Boundy, T. J. S. (1994). Pseudotachylytes generated during seismic faulting and eclogitization of the deep crust. *Science*, *265*(5168), 82–83. https://doi.org/10.1126/science.265.5168.82

Austrheim, H., & Griffin, W. L. (1985). Shear deformation and eclogite formation within granulite-facies anorthosites of the Bergen Arcs, western Norway. *Chemical Geology*, *50*(1–3), 267–281. https://doi.org/10.1016/0009-2541(85)90124-x

Behrens, H. (2021). Hydrogen defects in feldspars: Defect properties and implications for water solubility in feldspar. *Physics and Chemistry of Minerals*, *48*(2), 1–22. https://doi.org/10.1007/s00269-020-01128-0

Beinlich, A., John, T., Vrijmoed, J. C., Tominaga, M., Magna, T., & Podladchikov, Y. Y. (2020). Instantaneous rock transformations in the deep crust driven by reactive fluid flow. *Nature Geoscience*, *13*(4), 307–311. https://doi.org/10.1038/s41561-020-0554-9

Bhowany, K., Hand, M., Clark, C., Kelsey, D., Reddy, S., Pearce, M., et al. (2018). Phase equilibria modelling constraints on P–T conditions during fluid catalyzed conversion of granulite to eclogite in the Bergen Arcs, Norway. *Journal of Metamorphic Geology*, *36*(3), 315–342. https://doi.org/10.1111/jmg.12294

Boundy, T., Fountain, D., & Austrheim, H. (1992). Structural development and petrofabrics of eclogite facies shear zones, Bergen Arcs, western Norway: Implications for deep crustal deformational processes. *Contributions to Mineralogy and Petrology*, *10*(2), 127–146. https://doi.org/10.1111/j.1525-1314.1992.tb00075.x

Bras, E., Baïsset, M., Yamato, P., & Labrousse, L. (2021). Transient weakening during the granulite to eclogite transformation within hydrous shear zones (Holsnøy, Norway). *Tectonophysics*, *819*, 229026. https://doi.org/10.1016/j.tecto.2021.229026

Brodie, K., & Rutter, E. (1987). The role of transiently fine-grained reaction products in syntectonic metamorphism: Natural and experimental examples. *Canadian Journal of Earth Sciences*, *24*(3), 556–564. https://doi.org/10.1139/e87-054

Bucher, K., & Grapes, R. (2009). The eclogite-facies Allalin Gabbro of the Zermatt–Saas ophiolite, Western Alps: A record of subduction zone hydration. *Journal of Petrology*, *50*(8), 1405–1442. https://doi.org/10.1093/petrology/egp035

Bürgmann, R., & Dresen, G. (2008). Rheology of the lower crust and upper mantle: Evidence from rock mechanics, geodesy, and field observations. *Annual Review of Earth and Planetary Sciences*, *36*(1), 531–567. https://doi.org/10.1146/annurev.earth.36.031207.124326

Camacho, A., Lee, J. K., Hensen, B. J., & Braun, J. (2005). Short-lived orogenic cycles and the eclogitization of cold crust by spasmodic hot fluids. *Nature*, *435*(7046), 1191–1196. https://doi.org/10.1038/nature03643

Carreras, J., Cosgrove, J. W., & Druguet, E. (2013). Strain partitioning in banded and/or anisotropic rocks: Implications for inferring tectonic regimes. *Journal of Structural Geology*, *50*, 7–21. https://doi.org/10.1016/j.jsg.2012.12.003

Corfu, F., Andersen, T. B., & Gasser, D. (2014). The Scandinavian Caledonides: Main features, conceptual advances and critical questions. *Geological Society, London, Special Publications*, *390*(1), 9–43. https://doi.org/10.1144/SP390.25

Deer, W. A., Howie, R. A., & Zussman, J. (1997). Rock-forming minerals: Single-chain silicates (Vol. 2A).

De Ronde, A., Stünitz, H., Tullis, J., & Heilbronner, R. (2005). Reaction-induced weakening of plagioclase–olivine composites. *Tectonophysics*, *409*(1–4), 85–106. https://doi.org/10.1016/j.tecto.2005.08.008

Dohmen, R., & Milke, R. (2010). Diffusion in polycrystalline materials: Grain boundaries, mathematical models, and experimental data. *Reviews in Mineralogy and Geochemistry*, *72*(1), 921–970. https://doi.org/10.2138/rmg.2010.72.21

Fagereng, Å., & Biggs, J. (2019). New perspectives on 'geological strain rates' calculated from both naturally deformed and actively deforming rocks. *Journal of Structural Geology*, *125*, 100–110. https://doi.org/10.1016/j.jsg.2018.10.004

FitzGerald, J. D., & Stünitz, H. (1993). Deformation of granitoids at low metamorphic grade. I: Reactions and grain size reduction. *Tectonophysics*, *221*(3–4), 269–297. https://doi.org/10.1016/0040-1951(93)90163-e

Fossen, H., & Cavalcante, G. C. G. (2017). Shear zones–A review. *Earth-Science Reviews*, *171*, 434–455. https://doi.org/10.1016/j.earscirev.2017.05.002

Fossen, H., & Dunlap, W. J. (1998). Timing and kinematics of Caledonian thrusting and extensional collapse, southern Norway: Evidence from $^{40}Ar/^{39}Ar$ thermochronology. *Journal of Structural Geology*, *20*(6), 765–781. https://doi.org/10.1016/S0191-8141(98)00007-8

Fountain, D. M., Boundy, T. M., Austrheim, H., & Rey, P. (1994). Eclogite-facies shear zones—Deep crustal reflectors? *Tectonophysics*, *232*(1–4), 411–424. https://doi.org/10.1016/0040-1951(94)90100-7

Fusseis, F., Handy, M. R., & Schrank, C. (2006). Networking of shear zones at the brittle-to-viscous transition (Cap de Creus, NE Spain). *Journal of Structural Geology*, *28*(7), 1228–1243. https://doi.org/10.1016/j.jsg.2006.03.022

Fusseis, F., Regenauer-Lieb, K., Liu, J., Hough, R., & De Carlo, F. (2009). Creep cavitation can establish a dynamic granular fluid pump in ductile shear zones. *Nature*, *459*(7249), 974–977. https://doi.org/10.1038/nature08051

Gerya, T. (2019). *Introduction to numerical geodynamic modelling*. Cambridge University Press.

Giuntoli, F., Menegon, L., & Warren, C. J. (2018). Replacement reactions and deformation by dissolution and precipitation processes in amphibolites. *Journal of Metamorphic Geology*, *36*(9), 1263–1286. https://doi.org/10.1111/jmg.12445

Glodny, J., Kühn, A., & Austrheim, H. (2008). Geochronology of fluid-induced eclogite and amphibolite facies metamorphic reactions in a subduction–collision system, Bergen Arcs, Norway. *Contributions to Mineralogy and Petrology*, *156*(1), 27–48. https://doi.org/10.1007/s00410-007-0272-y

Gueydan, F., Leroy, Y., Jolivet, L., & Agard, P. (2003). Analysis of continental localization induced by reaction-softening and microfracturing. *Journal of Geophysical Research*, *108*(B2), 2064. https://doi.org/10.1029/2001jb000611

Guillot, S., Garzanti, E., Baratoux, D., Marquer, D., Mahéo, G., & de Sigoyer, J. (2003). Reconstructing the total shortening history of the NW Himalaya. *Geochemistry, Geophysics, Geosystems*, *4*(7), 1064. https://doi.org/10.1029/2002gc000484

Hacker, B. R., Andersen, T. B., Johnston, S., Kylander-Clark, A. R., Peterman, E. M., Walsh, E. O., & Young, D. (2010). High-temperature deformation during continental-margin subduction & exhumation: The ultrahigh-pressure Western Gneiss Region of Norway. *Tectonophysics*, *480*(1–4), 149–171. https://doi.org/10.1016/j.tecto.2009.08.012

Halter, W. R., Macherel, E., & Schmalholz, S. M. (2022). A simple computer program for calculating stress and strain rate in 2D viscous inclusion-matrix systems. *Journal of Structural Geology*, *160*, 104617. https://doi.org/10.1016/j.jsg.2022.104617

Handy, M. R. (1989). Deformation regimes and the rheological evolution of fault zones in the lithosphere: The effects of pressure, temperature, grainsize and time. *Tectonophysics*, *163*(1–2), 119–152. https://doi.org/10.1016/0040-1951(89)90122-4

Herwegh, M., Berger, A., Ebert, A., & Brodhag, S. (2008). Discrimination of annealed and dynamic fabrics: Consequences for strain localization and deformation episodes of large-scale shear zones. *Earth and Planetary Science Letters*, *276*(1–2), 52–61. https://doi.org/10.1016/j.epsl.2008.09.007

Hobbs, B., Regenauer-Lieb, K., & Ord, A. (2008). Folding with thermal–mechanical feedback. *Journal of Structural Geology*, *30*(12), 1572–1592. https://doi.org/10.1016/j.jsg.2008.09.002

Huet, B., Yamato, P., & Grasemann, B. (2014). The Minimized Power Geometric model: An analytical mixing model for calculating polyphase rock viscosities consistent with experimental data. *Journal of Geophysical Research: Solid Earth*, *119*(4), 3897–3924. https://doi.org/10.1002/2013jb010453

Incel, S., Labrousse, L., Hilairet, N., John, T., Gasc, J., Shi, F., et al. (2019). Reaction-induced embrittlement of the lower continental crust. *Geology*, *47*(3), 235–238. https://doi.org/10.1130/g45527.1

Ingrin, J., & Blanchard, M. (2006). Diffusion of hydrogen in minerals. *Reviews in Mineralogy and Geochemistry*, *62*(1), 291–320. https://doi.org/10.2138/rmg.2006.62.13

Jackson, J. A., Austrheim, H., McKenzie, D., & Priestley, K. (2004). Metastability, mechanical strength, and the support of mountain belts. *Geology*, *32*(7), 625. https://doi.org/10.1130/g20397.1

Jakob, J., Alsaif, M., Corfu, F., & Andersen, T. B. (2017). Age and origin of thin discontinuous gneiss sheets in the distal domain of the magma-poor hyperextended pre-Caledonian margin of Baltica, southern Norway. *Journal of the Geological Society*, *174*(3), 557–571. https://doi.org/10.1144/jgs2016-049

Jamtveit, B., Ben-Zion, Y., Renard, F., & Austrheim, H. (2018). Earthquake-induced transformation of the lower crust. *Nature*, *556*(7702), 487–491. https://doi.org/10.1029/2018JB016461

Jamtveit, B., Bucher-Nurminen, K., & Austrheim, H. (1990). Fluid controlled eclogitization of granulites in deep crustal shear zones, Bergen arcs, western Norway. *Contributions to Mineralogy and Petrology*, *104*(2), 184–193. https://doi.org/10.1007/bf00306442

Jamtveit, B., Dunkel, K. G., Petley-Ragan, A., Austrheim, H., Corfu, F., & Schmid, D. W. (2021). Rapid fluid-driven transformation of lower continental crust associated with thrust-induced shear heating. *Lithos*, *396*, 106216. https://doi.org/10.1016/j.lithos.2021.106216

Jamtveit, B., Moulas, E., Andersen, T. B., Austrheim, H., Corfu, F., Petley-Ragan, A., & Schmalholz, S. M. (2018). High pressure metamorphism caused by fluid induced weakening of deep continental crust. *Scientific Reports*, *8*(1), 17011. https://doi.org/10.1038/s41598-018-35200-1

Jamtveit, B., Petley-Ragan, A., Incel, S., Dunkel, K. G., Aupart, C., Austrheim, H., et al. (2019). The effects of earthquakes and fluids on the metamorphism of the lower continental crust. *Journal of Geophysical Research: Solid Earth*, *124*(8), 7725–7755. https://doi.org/10.1029/2018JB016461

John, T., Gussone, N., Podladchikov, Y. Y., Bebout, G. E., Dohmen, R., Halama, R., et al. (2012). Volcanic arcs fed by rapid pulsed fluid flow through subducting slabs. *Nature Geoscience*, *5*(7), 489–492. https://doi.org/10.1038/ngeo1482

John, T., & Schenk, V. (2003). Partial eclogitisation of gabbroic rocks in a late Precambrian subduction zone (Zambia): Prograde metamorphism triggered by fluid infiltration. *Contributions to Mineralogy and Petrology*, *146*(2), 174–191. https://doi.org/10.1007/s00410-003-0492-8

Jolivet, L., Raimbourg, H., Labrousse, L., Avigad, D., Leroy, Y., Austrheim, H., & Andersen, T. B. (2005). Softening trigerred by eclogitization, the first step toward exhumation during continental subduction. *Earth and Planetary Science Letters*, *237*(3–4), 532–547. https://doi.org/10.1016/j.epsl.2005.06.047

Kaatz, L., Reynes, J., Hermann, J., & John, T. (2022). How fluid infiltrates dry crustal rocks during progressive eclogitization and shear zone formation: Insights from H_2O contents in nominally anhydrous minerals. *Contributions to Mineralogy and Petrology*, *177*(7), 1–20. https://doi.org/10.1007/s00410-022-01938-1

Kaatz, L., Zertani, S., Moulas, E., John, T., Labrousse, L., Schmalholz, S. M., & Andersen, T. B. (2021). Widening of hydrous shear zones during incipient eclogitization of metastable dry and rigid lower crust—Holsnøy, western Norway. *Tectonics*, *40*(3). https://doi.org/10.1029/2020TC006572

Katayama, I., & Karato, S.-I. (2008). Effects of water and iron content on the rheological contrast between garnet and olivine. *Physics of the Earth and Planetary Interiors*, *166*(1–2), 57–66. https://doi.org/10.1016/j.pepi.2007.10.004

Klemd, R., John, T., Scherer, E. E., Rondenay, S., & Gao, J. (2011). Changes in dip of subducted slabs at depth: Petrological and geochronological evidence from HP–UHP rocks (Tianshan, NW-China). *Earth and Planetary Science Letters*, *310*(1–2), 9–20. https://doi.org/10.1016/j.epsl.2011.07.022

Kohlstedt, D. L., & Mackwell, S. J. (1998). Diffusion of hydrogen and intrinsic point defects in olivine. *Zeitschrift für Physikalische Chemie*, *207*(1–2), 147–162. https://doi.org/10.1524/zpch.1998.207.part_1_2.147

Labrousse, L., Hetényi, G., Raimbourg, H., Jolivet, L., & Andersen, T. B. (2010). Initiation of crustal-scale thrusts triggered by metamorphic reactions at depth: Insights from a comparison between the Himalayas and Scandinavian Caledonides. *Tectonics*, *29*(5). https://doi.org/10.1029/2009tc002602

Lasaga, A. C. (1998). *Kinetic theory in the earth sciences*. Princeton University Press.

Lasaga, A. C., & Blum, A. E. (1986). Surface chemistry, etch pits and mineral-water reactions. *Geochimica et Cosmochimica Acta*, *50*(10), 2363–2379. https://doi.org/10.1016/0016-7037(86)90088-8

Li, Z. (2014). A review on the numerical geodynamic modeling of continental subduction, collision and exhumation. *Science China Earth Sciences*, *57*(1), 47–69. https://doi.org/10.1007/s11430-013-4696-0

Llana-Fúnez, S., Wheeler, J., & Faulkner, D. R. (2012). Metamorphic reaction rate controlled by fluid pressure not confining pressure: Implications of dehydration experiments with gypsum. *Contributions to Mineralogy and Petrology*, *164*(1), 69–79. https://doi.org/10.1007/s00410-012-0726-8

Mackwell, S. J., Bai, Q., & Kohlstedt, D. (1990). Rheology of olivine and the strength of the lithosphere. *Geophysical Research Letters*, *17*(1), 9–12. https://doi.org/10.1029/gl017i001p00009

Mackwell, S. J., Kohlstedt, D., & Paterson, M. (1985). The role of water in the deformation of olivine single crystals. *Journal of Geophysical Research*, *90*(B13), 11319–11333. https://doi.org/10.1029/jb090ib13p11319

Mackwell, S. J., & Kohlstedt, D. L. (1990). Diffusion of hydrogen in olivine: Implications for water in the mantle. *Journal of Geophysical Research*, *95*(B4), 5079–5088. https://doi.org/10.1029/jb095ib04p05079

Malvoisin, B., Austrheim, H., Hetényi, G., Reynes, J., Hermann, J., Baumgartner, L. P., & Podladchikov, Y. Y. (2020). Sustainable densification of the deep crust. *Geology*, *48*(7), 673–677. https://doi.org/10.1130/g47201.1

Malvoisin, B., Podladchikov, Y. Y., & Vrijmoed, J. C. (2015). Coupling changes in densities and porosity to fluid pressure variations in reactive porous fluid flow: Local thermodynamic equilibrium. *Geochemistry, Geophysics, Geosystems*, *16*(12), 4362–4387. https://doi.org/10.1002/2015gc006019

Mancktelow, N. S., & Pennacchioni, G. (2005). The control of precursor brittle fracture and fluid–rock interaction on the development of single and paired ductile shear zones. *Journal of Structural Geology*, *27*(4), 645–661. https://doi.org/10.1016/j.jsg.2004.12.001

Manning, C. E. (2004). The chemistry of subduction-zone fluids. *Earth and Planetary Science Letters*, *223*(1–2), 1–16. https://doi.org/10.1016/j.epsl.2004.04.030

Manning, C. E., & Frezzotti, M. L. (2020). Subduction-zone fluids. *Elements: An International Magazine of Mineralogy, Geochemistry, and Petrology*, *16*(6), 395–400. https://doi.org/10.2138/gselements.16.6.395

Marti, S., Stünitz, H., Heilbronner, R., Plümper, O., & Kilian, R. (2018). Syn-kinematic hydration reactions, grain size reduction, and dissolution–precipitation creep in experimentally deformed plagioclase–pyroxene mixtures. *Solid Earth*, *9*(4), 985–1009. https://doi.org/10.5194/se-9-985-2018

Mattey, D., Jackson, D., Harris, N., & Kelley, S. (1994). Isotopic constraints on fluid infiltration from an eclogite facies shear zone, Holsenøy, Norway. *Journal of Metamorphic Geology*, *12*(3), 311–325. https://doi.org/10.1111/j.1525-1314.1994.tb00025.x

Menegon, L., Pennacchioni, G., Malaspina, N., Harris, K., & Wood, E. (2017). Earthquakes as precursors of ductile shear zones in the dry and strong lower crust. *Geochemistry, Geophysics, Geosystems*, *18*(12), 4356–4374. https://doi.org/10.1002/2017gc007189

Menegon, L., Pennacchioni, G., & Spiess, R. (2008). Dissolution-precipitation creep of K-feldspar in mid-crustal granite mylonites. *Journal of Structural Geology*, *30*(5), 565–579. https://doi.org/10.1016/j.jsg.2008.02.001

Moore, J., Beinlich, A., Austrheim, H., & Putnis, A. (2019). Stress orientation–dependent reactions during metamorphism. *Geology*, *47*(2), 151–154. https://doi.org/10.1130/g45632.1

Mosenfelder, J. L., Rossman, G. R., & Johnson, E. A. (2015). Hydrous species in feldspars: A reassessment based on FTIR and SIMS. *American Mineralogist*, *100*(5–6), 1209–1221. https://doi.org/10.2138/am-2015-5034

Moulas, E., Kaus, B., & Jamtveit, B. (2022). Dynamic pressure variations in the lower crust caused by localized fluid-induced weakening. *Communications Earth & Environment*, *3*(1), 157. https://doi.org/10.1038/s43247-022-00478-7

Mukai, H., Austrheim, H., Putnis, C. V., & Putnis, A. (2014). Textural evolution of plagioclase feldspar across a shear zone: Implications for deformation mechanism and rock strength. *Journal of Petrology*, *55*(8), 1457–1477. https://doi.org/10.1093/petrology/egu030

Oliot, E., Goncalves, P., & Marquer, D. (2010). Role of plagioclase and reaction softening in a metagranite shear zone at mid-crustal conditions (Gotthard Massif, Swiss Central Alps). *Journal of Metamorphic Geology*, *28*(8), 849–871. https://doi.org/10.1111/j.1525-1314.2010.00897.x

Padrón-Navarta, J. A., Hermann, J., & O'Neill, H. S. C. (2014). Site-specific hydrogen diffusion rates in forsterite. *Earth and Planetary Science Letters*, *392*, 100–112. https://doi.org/10.1016/j.epsl.2014.01.055

Pennacchioni, G., & Mancktelow, N. S. (2007). Nucleation and initial growth of a shear zone network within compositionally and structurally heterogeneous granitoids under amphibolite facies conditions. *Journal of Structural Geology*, *29*(11), 1757–1780. https://doi.org/10.1016/j.jsg.2007.06.002

Petley-Ragan, A., Dunkel, K. G., Austrheim, H., Ildefonse, B., & Jamtveit, B. (2018). Microstructural records of earthquakes in the lower crust and associated fluid-driven metamorphism in plagioclase-rich granulites. *Journal of Geophysical Research: Solid Earth*, *123*(5), 3729–3746. https://doi.org/10.1029/2017JB015348

Piccoli, F., Hermann, J., Pettke, T., Connolly, J., Kempf, E. D., & Duarte, J. V. (2019). Subducting serpentinites release reduced, not oxidized, aqueous fluids. *Scientific Reports*, *9*(1), 1–7. https://doi.org/10.1038/s41598-019-55944-8

Plümper, O., Botan, A., Los, C., Liu, Y., Malthe-Sørenssen, A., & Jamtveit, B. (2017). Fluid-driven metamorphism of the continental crust governed by nanoscale fluid flow. *Nature Geoscience*, *10*(9), 685–690. https://doi.org/10.1038/ngeo3009

Pollard, D., & Fletcher, R. C. (2005). *Fundamentals of structural geology*. Cambridge University Press.

Putnis, A. (2021). Fluid–mineral interactions: Controlling coupled mechanisms of reaction, mass transfer and deformation. *Journal of Petrology*, *62*(12), egab092. https://doi.org/10.1093/petrology/egab092

Putnis, A., & Austrheim, H. (2010). Fluid-induced processes: Metasomatism and metamorphism. *Geofluids*. https://doi.org/10.1111/j.1468-8123.2010.00285.x

Putnis, A., & John, T. (2010). Replacement processes in the Earth's crust. *Elements*, *6*(3), 159–164. https://doi.org/10.2113/gselements.6.3.159

Raimbourg, H., Jolivet, L., Labrousse, L., Leroy, Y., & Avigad, D. (2005). Kinematics of syneclogite deformation in the Bergen Arcs, Norway: Implications for exhumation mechanisms. *Geological Society, London, Special Publications*, *243*(1), 175–192. https://doi.org/10.1144/GSL.SP.2005.243.01.13

Raimbourg, H., Jolivet, L., & Leroy, Y. (2007). Consequences of progressive eclogitization on crustal exhumation, a mechanical study. *Geophysical Journal International*, *168*(1), 379–401. https://doi.org/10.1111/j.1365-246X.2006.03130.x

Reynes, J., Jollands, M., Hermann, J., & Ireland, T. (2018). Experimental constraints on hydrogen diffusion in garnet. *Contributions to Mineralogy and Petrology*, *173*(9), 69. https://doi.org/10.1007/s00410-018-1492-z

Roberts, D. (2003). The Scandinavian Caledonides: Event chronology, palaeogeographic settings and likely modern analogues. *Tectonophysics*, *365*(1–4), 283–299. https://doi.org/10.1016/S0040-1951(03)00026-X

Rubie, D. C. (1983). Reaction-enhanced ductility: The role of solid-solid univariant reactions in deformation of the crust and mantle. *Tectonophysics*, *96*(3–4), 331–352. https://doi.org/10.1016/0040-1951(83)90225-1

Rybacki, E., & Dresen, G. (2000). Dislocation and diffusion creep of synthetic anorthite aggregates. *Journal of Geophysical Research*, *105*(B11), 26017–26036. https://doi.org/10.1029/2000jb900223

Rybacki, E., & Dresen, G. (2004). Deformation mechanism maps for feldspar rocks. *Tectonophysics*, *382*(3–4), 173–187. https://doi.org/10.1016/j.tecto.2004.01.006

Schneider, F., Yuan, X., Schurr, B., Mechie, J., Sippl, C., Haberland, C., et al. (2013). Seismic imaging of subducting continental lower crust beneath the Pamir. *Earth and Planetary Science Letters*, *375*, 101–112. https://doi.org/10.1016/j.epsl.2013.05.015

Schrank, C., Handy, M., & Fusseis, F. (2008). Multiscaling of shear zones and the evolution of the brittle-to-viscous transition in continental crust. *Journal of Geophysical Research*, *113*(B1), B01407. https://doi.org/10.1029/2006jb004833

Stalder, R., Purwin, H., & Skogby, H. (2007). Influence of Fe on hydrogen diffusivity in orthopyroxene. *European Journal of Mineralogy*, *19*(6), 899–903. https://doi.org/10.1127/0935-1221/2007/0019-1780

Stünitz, H., Neufeld, K., Heilbronner, R., Finstad, A. K., Konopásek, J., & Mackenzie, J. R. (2020). Transformation weakening: Diffusion creep in eclogites as a result of interaction of mineral reactions and deformation. *Journal of Structural Geology*, *139*, 104129. https://doi.org/10.1016/j.jsg.2020.104129

Stünitz, H., Thust, A., Heilbronner, R., Behrens, H., Kilian, R., Tarantola, A., & Fitz Gerald, J. (2017). Water redistribution in experimentally deformed natural milky quartz single crystals—Implications for H_2O-weakening processes. *Journal of Geophysical Research: Solid Earth*, *122*(2), 866–894. https://doi.org/10.1002/2016jb013533

Syracuse, E. M., van Keken, P. E., & Abers, G. A. (2010). The global range of subduction zone thermal models. *Physics of the Earth and Planetary Interiors*, *183*(1–2), 73–90. https://doi.org/10.1016/j.pepi.2010.02.004

Taetz, S., John, T., Bröcker, M., Spandler, C., & Stracke, A. (2018). Fast intraslab fluid-flow events linked to pulses of high pore fluid pressure at the subducted plate interface. *Earth and Planetary Science Letters*, *482*, 33–43. https://doi.org/10.1016/j.epsl.2017.10.044

Terry, M. P., & Heidelbach, F. (2006). Deformation-enhanced metamorphic reactions and the rheology of high-pressure shear zones, Western Gneiss Region, Norway. *Journal of Metamorphic Geology*, *24*(1), 3–18. https://doi.org/10.1111/j.1525-1314.2005.00618.x

Tielke, J. A., Zimmerman, M. E., & Kohlstedt, D. L. (2017). Hydrolytic weakening in olivine single crystals. *Journal of Geophysical Research: Solid Earth*, *122*(5), 3465–3479. https://doi.org/10.1002/2017jb014004

Tollan, P., & Hermann, J. (2019). Arc magmas oxidized by water dissociation and hydrogen incorporation in orthopyroxene. *Nature Geoscience*, *12*(8), 667–671. https://doi.org/10.1038/s41561-019-0411-x

Tollan, P. M., O'Neill, H. S. C., & Hermann, J. (2018). The role of trace elements in controlling H incorporation in San Carlos olivine. *Contributions to Mineralogy and Petrology*, *173*(11), 1–23. https://doi.org/10.1007/s00410-018-1517-7

Tullis, J., & Yund, R. A. (1985). Dynamic recrystallization of feldspar: A mechanism for ductile shear zone formation. *Geology*, *13*(4), 238–241. https://doi.org/10.1130/0091-7613(1985)13%3C238:DROFAM%3E2.0.CO;2

Turcotte, D. L., & Schubert, G. (2014). *Geodynamics*. Cambridge University Press.

Wain, A., Waters, D., & Austrheim, H. (2001). Metastability of granulites and processes of eclogitisation in the UHP region of western Norway. *Journal of Metamorphic Geology*, *19*(5), 609–625. https://doi.org/10.1046/j.0263-4929.2001.00333.x

Wayte, G. J., Worden, R. H., Rubie, D. C., & Droop, G. T. (1989). A TEM study of disequilibrium plagioclase breakdown at high pressure: The role of infiltrating fluid. *Contributions to Mineralogy and Petrology*, *101*(4), 426–437. https://doi.org/10.1007/bf00372216

Wehrens, P., Baumberger, R., Berger, A., & Herwegh, M. (2017). How is strain localized in a meta-granitoid, mid-crustal basement section? Spatial distribution of deformation in the central Aar massif (Switzerland). *Journal of Structural Geology*, *94*, 47–67. https://doi.org/10.1016/j.jsg.2016.11.004

Yuan, X., Sobolev, S. V., Kind, R., Oncken, O., Bock, G., Asch, G., et al. (2000). Subduction and collision processes in the Central Andes constrained by converted seismic phases. *Nature*, *408*(6815), 958–961. https://doi.org/10.1038/35050073

Zertani, S., John, T., Brachmann, C., Vrijmoed, J. C., & Plümper, O. (2022). Reactive fluid flow guided by grain-scale equilibrium reactions during eclogitization of dry crustal rocks. *Contributions to Mineralogy and Petrology*, *177*(6), 1–18. https://doi.org/10.1007/s00410-022-01928-3

Zertani, S., Labrousse, L., John, T., Andersen, T. B., & Tilmann, F. (2019). The interplay of eclogitization and deformation during deep burial of the lower continental crust—A case study from the Bergen Arcs (Western Norway). *Tectonics*, *38*(3), 898–915. https://doi.org/10.1029/2018tc005297

Zheng, Y.-F., & Hermann, J. (2014). Geochemistry of continental subduction-zone fluids. *Earth Planets and Space*, *66*(1), 1–16. https://doi.org/10.1186/1880-5981-66-93